N O T I C E

THIS DOCUMENT HAS BEEN REPRODUCED FROM MICROFICHE. ALTHOUGH IT IS RECOGNIZED THAT CERTAIN PORTIONS ARE ILLEGIBLE, IT IS BEING RELEASED IN THE INTEREST OF MAKING AVAILABLE AS MUCH INFORMATION AS POSSIBLE

024

CORNELL UNIVERSITY

Center for Radiophysics and Space Research

ITHACA, N. Y.

STELLAR CONVECTION II:

A MULTI-MODE NUMERICAL SOLUTION FOR

CONVECTION IN SPHERES

Philip S. Marcus

STELLAR CONVECTION II:

A MULTI-MODE NUMERICAL SOLUTION FOR

CONVECTION IN SPHERES[*]

Philip S. Marcus

Center for Radiophysics and Space Research

Cornell University

November 1979

ABSTRACT

We have computed a stable, equilibrium solution for convection in a self-gravitating sphere of Boussinesq fluid by using a modal analysis in which the θ, ϕ dependence of the fluid is expanded in the set of 168 spherical harmonics, $Y^{\ell,m}$, with $\ell \leq 12$. To compute the numerical solution of our hierarchy of nonlinearly coupled equations, we have developed a new relaxation method. For a Rayleigh number that is ~ 30 times critical and a Prandtl number of 10, the flow has two orthogonal planes of reflection symmetry. The temperature, velocity and convective flux of the fluid as well as the kinetic and thermal energy spectra as functions of wavelength are computed. The spectra are found to be in agreement with both experimental observations and analytic scaling laws. We examine the dynamics of the energy cascade by computing the ratio of the amount of energy dissipation at a particular wavelength to the amount of energy produced at that same wavelength. We find that there is only a slight cascade of kinetic energy to smaller wavelengths but a large cascade of thermal energy. The fraction of the convective flux that is carried by each wavelength and the degree of anisotropy associated with each lengthscale are also determined. The stable, steady-state convecting fluid has a rotation law such that the angular momentum per unit mass as a function of radius is constant.

Subject headings: convection - stars: interiors - hydrodynamics

I. INTRODUCTION

Thermal convection is perhaps the most important unsolved problem in stellar structure. In 1916 Lord Rayleigh determined the necessary conditions for convective instability using linear theory. Since then, people have been trying to calculate stable, equilibrium solutions to the nonlinear equations of motion. One of the most successful methods is finite amplitude theory (Malkus and Veronis, 1958), which can be used to predict the convective flux and temperature gradient for mildly nonlinear, low Reynolds number flows. Recently, Busse (1975) has computed time-independent convective patterns in spheres and spherical shells using this method. Lorenz (1963) considered the self-interaction of a single mode whose radial and horizontal structure was fixed for all time but whose amplitude was allowed to vary. He was able to compute a seemingly "turbulent" time dependence for the convective flux. Toomre et al (1977) have also computed nonlinear solutions by using a single mode whose horizontal structure is fixed but whose vertical structure is determined by the equations of motion. They have been able to calculate convective fluxes that have been applied to the second convection zone of an A star (1976). Each of these nonlinear methods has produced interesting results, but they are all, obviously, limited to low Reynolds number flows. A severe problem inherent in each method is that it requires a priori knowledge of the horizontal structure of the flow. It cannot be determined with these methods which, if any, of the infinite number of possible equilibrium solutions is stable. It is clearly desirable to compare the results of these

nonlinear analyses with the solution of a high spatial resolution numerical computation.

In this paper we numerically determine the convective flow of a self-gravitating sphere of Boussinesq fluid for small Reynolds and Peclet numbers. We use the 3-dimensional modal analysis that was developed by this author in a previous paper (1979, hereafter referred to as Paper I). Although the small Reynolds and Peclet numbers are not appropriate for astrophysical flows, their smallness enables us to numerically resolve all of the important physical lengthscales. This paper is necessary as a foil for the following paper in which we calculate convection for large Reynolds and Peclet numbers, but model the flow at small lengthscales. The decomposition of the equations of motion into modes is reviewed in §2 of this paper and a relaxation method that allows us to compute solutions to these equations is presented in §3. With this Galerkin method, we are not restricted to small perturbations. By using a wide range of initial conditions and showing that they always evolve to the same steady-state, we determine the stable equilibrium flow for a Rayleigh number of 10^4 and a Prandtl number of 10.

In §3 we derive different measures that can be used to describe the over-all properties of this flow. The 2 and 3-dimensional spectra of the kinetic and thermal energies and the convective flux as a function of wavelengths are calculated in terms of modes. We also define a measure of the anisotropy of the flow as a function of wavelength. In §4 we present the results of our numerical calculations for our stable convective solution in terms of these measures. Our discussion is in §6.

II. MODAL EQUATIONS FOR CONVECTION

A. Galerkin Decomposition

The modal equations governing convection in a self-gravitating sphere of Boussinesq fluid were derived in Paper I. In these equations the solenoidal velocity is written as a sum of its poloidal part, $\underline{v}_p$, and its toroidal part, $\underline{v}_T$, which are derived from the scalar fields ω and ψ.

$$\underline{v}_p = \nabla \left[\partial(r\omega)/\partial r\right] - (r\nabla^2 \omega)\,\hat{e}_r \tag{2.1}$$

$$\underline{v}_T = r\nabla \times (\psi\hat{e}_r) \tag{2.2}$$

Each scalar function, $f(r,\theta,\phi,t)$ is written as a sum of its mean or horizontally averaged part, $<f(r)>$, and its fluctuating part, $\tilde{f} \equiv f - <f>$ where

$$<f(r,t)> = \int_{4\pi} d\Omega \; f(r,\theta,\phi,t) \,/4\pi \tag{2.3}$$

The fluctuation, $\tilde{f}$, is written as a truncated Galerkin expansion using spherical harmonics:

$$\tilde{f}(r,\theta,\phi,t) =$$

$$\sum_{\ell=1}^{\ell_{cutoff}} \sum_{m,\gamma} f_{\gamma,\ell,m}(r,t) \; Y^{\gamma,\ell,m}(\theta,\phi) \tag{2.4}$$

where

$$Y^{R,\ell,m} = \begin{cases} 2(2\pi)^{1/2} \; \text{Re} \; (Y^{\ell,m}) & m \neq 0 \\ 2(\pi)^{1/2} \; Y^{\ell,0} & m = 0 \end{cases} \tag{2.5}$$

$$Y^{I,\ell,m} = \begin{cases} 2(2\ )^{1/2} \; \text{Im} \; (Y^{\ell,m}) & m \neq 0 \\ 0 & m = 0 \end{cases} \tag{2.6}$$

and where $\text{Re}(Y^{\ell,m})$ and $\text{Im}(Y^{\ell,m})$ are the real and imaginary parts of the spherical harmonic. The second sum in equation (2.4) is over $0 \leq m \leq \ell$ and $\gamma = R$ and I. The Galerkin truncation is made by restricting the first sum in equation (2.4) to $\ell \leq \ell_{cutoff}$. We adopt the notation that $<<f(r)>>$ is the stationary value of $<f(r,t)>$; that is, if τ is a period of time that is long compared to the timescales over which $<f(r,t)>$ changes, then

$$<<f(r)>> \equiv \frac{1}{\tau} \int_0^\tau <f(r,t)> \, dt \qquad (2.7)$$

If the value of $<<f>>$ depends upon the origin of time used on the right-hand side of eq.(2.7), then $<f(r,t)>$ is not a stationary function and $<<f>>$ is undefined.

We shall consider a Boussinesq fluid with a thermal expansion coefficient, α, a kinematic viscosity, ν, heat capacity c_p, a thermal diffusivity, k, and a mean density ρ. The heat source is $H(r)$ and the steady-state luminosity, $\mathcal{L}(r)$, is

$$\mathcal{L}(r) = 4\pi \int_0^r <H> \, r'^2 \, dr' \qquad (2.8)$$

We non-dimensionalize the equations of motion by using the radius of sphere, R, as the unit of length, ρR^3 as the unit of mass, R^2/k as the unit of time, and $\mathcal{L}(R)/4\pi\rho c_p R k$ as the unit of temperature. In these units the equations that govern the velocity, temperature, T, pressure, P, and gravitational potential, Φ, are:

$$\partial \omega_{\gamma,\ell,m} / \partial t =$$

$$-r \, [\ell(\ell+1)]^{-1} \, [R_s P_r r \, T_{\gamma,\ell,m} + \partial \, (P_{\gamma,\ell,m} + \Phi_{\gamma,\ell,m})/\partial r]$$

$$+ P_r \, \mathcal{D}_\ell \, (\omega_{\gamma,\ell,m})$$

$$- \ell(\ell+1)^{-1} \, \{r \, \hat{e}_r \cdot [(\underline{v}\cdot\nabla)\underline{v}]\}_{\gamma,\ell,m} \qquad (2.9)$$

$$\partial \psi_{\gamma,\ell,m} / \partial t = P_r \, \mathcal{D}_\ell \, (\psi_{\gamma,\ell,m})$$

$$-\ell(\ell+1)^{-1} \, \{r \, \hat{e}_r \cdot \nabla \times [(\underline{v}\cdot\nabla)\underline{v}]\}_{\gamma,\ell,m} \qquad (2.10)$$

$$\partial \, T_{\gamma,\ell,m} / \partial t = \mathcal{D}_\ell \, (T_{\gamma,\ell,m})$$

$$- \ell(\ell+1) \ (\partial <T>/\partial r) \ \omega_{\gamma,\ell,m}/r$$

$$- [\underline{v} \cdot \nabla T]_{\gamma,\ell,m} \tag{2.11}$$

$$\mathscr{D}_\ell \ (P_{\gamma,\ell,m}) = P_r \ R_s \ (6T_{\gamma,\ell,m} + r\partial T_{\gamma,\ell,m}/\partial r)$$

$$- r^{-2}\partial \ \{r[r \ \hat{e}_r \cdot (\underline{v}\cdot\nabla)\underline{v}]_{\gamma,\ell,m}\}/\partial r$$

$$- \{\nabla \cdot [(\underline{v} \cdot \nabla)\underline{v}]\}_{\gamma,\ell,m} \tag{2.12}$$

$$\mathscr{D}_\ell \ (\Phi_{\gamma,\ell,m}) = -3 \ P_r \ R_s \ T_{\gamma,\ell,m} \tag{2.13}$$

$$< \omega > \ = \ < \psi > \ = \ 0 \tag{2.14}$$

$$\frac{\partial <T>}{\partial t} = r^{-2}\{\partial(r^2\partial<T>/\partial r)/\partial r + \partial \mathscr{L}/\partial r$$

$$-\partial \ [\sum_{\gamma,\ell,m} r \ \ell(\ell+1) \ T_{\gamma,\ell,m} \ \omega_{\gamma,\ell,m}] \ / \ \partial r\} \tag{2.15}$$

where $\mathscr{D}_\ell$ is the second-order differential operator defined by its action on f,

$$\mathscr{D}_\ell \ (f) \equiv [\partial^2(rf)/\partial r^2 - \ell(\ell+1) \ f/r]/r \tag{2.16}$$

The subscript, γ, stands for either I or R. The nonlinear terms $\{r \ \hat{e}_r \cdot \nabla \times [(\underline{v}\cdot\nabla)\underline{v}]\}_{\gamma,\ell,m}, [(\underline{v}\cdot\nabla)T]_{\gamma,\ell,m}, [\hat{e}_r r\cdot(\underline{v}\cdot\nabla)\underline{v}]_{\gamma,\ell,m}$ and $\nabla\cdot[(\underline{v}\cdot\nabla)\underline{v}]_{\gamma,\ell,m}$ are explicitly expressed in terms of $\omega_{\gamma,\ell,m}$, $\psi_{\gamma,\ell,m}$, and $T_{\gamma,\ell,m}$ in Paper I. The Prandtl number, $Pr\equiv\nu/\mathscr{L}$, and the Rayleigh number, $Rs \equiv \alpha GR^3\mathscr{L}(R)/3\mathscr{L}^2\nu c_p$ (where G is the gravitational constant) are the two constants that appear in equations (2.3)-(2.15).

B. Boundary and Initial Conditions

The boundary conditions are that the surface of the convecting fluid is impermeable and stress-free. This requires that:

$$\omega_{\gamma,\ell,m}(1) = 0 \qquad (2.17)$$

$$\partial^2 \omega_{\gamma,\ell,m} / \partial r^2 \big|_{r=1} = 0 \qquad (2.18)$$

$$\partial(\psi_{\gamma,\ell,m} / r)/\partial r \big|_{r=1} = 0 \qquad (2.19)$$

The surface has no thermal resistivity and is therefore isothermal, or

$$T_{\gamma,\ell,m}(1) = 0 \qquad (2.20)$$

We are also free to fix $\langle T \rangle$ to be constant for all time at the surface. Since the specific value of $\langle T(1) \rangle$ has no effect on $\underline{v}$, $\tilde{T}$, $\tilde{P}$, $\tilde{\Phi}$, or $\partial \langle T \rangle/\partial r$, we set it equal to zero.

$$\langle T(1) \rangle = 0 \qquad (2.21)$$

We have chosen the heat source so that it has a constant value for $r \leq 0.3$ and is zero outside $r = 0.3$. In dimensionless units

$$\tilde{H} = 0 \qquad (2.22)$$

$$\langle H \rangle = \begin{cases} 3 / 4\pi(.3)^3 & r \leq 0.3 \\ 0 & r > 0.3 \end{cases} \qquad (2.23)$$

This heat source produces a steady state luminosity

$$\mathcal{L}(r) = \begin{cases} (r/.3)^3 & r \leq 0.3 \\ 1 & r > 0.3 \end{cases} \qquad (2.24)$$

The total heat flux (per unit area) at the surface is
$-\partial \langle T \rangle / \partial r$ and is free to vary in time. The thermal and kinetic
energy can be stored in the fluid and released through the sur-
face in a series of bursts rather than in a continuous flow.
However, $\langle\langle \partial T / \partial r \rangle\rangle = -1$.

No boundary conditions are imposed at the center of the
sphere, but regularity requires that leading order terms of
$\omega_{\gamma,\ell,m}$, $\psi_{\gamma,\ell,m}$, $T_{\gamma,\ell,m}$, $P_{\gamma,\ell,m}$, and $\phi_{\gamma,\ell,m}$ all go as r^{ℓ} at the
origin. The dipole component of the velocity may be nonzero
at $r = 0$.

III. ARTIFICIAL TIME METHOD OF SOLUTION

A straightforward method of obtaining solutions to equa-
tions (2.9) - (2.15) is to choose some initial data and inte-
grate the equations forward in time. However we have developed
a relaxation scheme, the method of artificial time, that deter-
mines convective solutions in a more efficient manner.

A. The Initial-Value Problem In Real Time

Consider a fluid with its mean temperature in conductive
equilibrium,

$$\langle T \rangle = \left\{ \begin{array}{ll} r/(.3)^3 & r \leq 0.3 \\ 1/r^2 & r > 0.3 \end{array} \right\} \qquad (3.1)$$

and with velocity and temperature fluctuations that are ini-
tially small. If the Rayleigh number is sufficiently large, ω and
T initially grow almost exponentially. We can understand this
growth by computing the linearized eigenmodes to equations (2.9)

- (2.15); $\omega_{\gamma,\ell,m}$ and $T_{\gamma,\ell,m}$ grow (decay) if Rs is greater (less)

than the critical Rayleigh number, $Rs_{crit}(\ell)$. The growth or decay

rates are independent of γ and m. The toroidal component of

the velocity always decays initially. $Rs_{crit}(\ell)$ is given in

table 3.1.

TABLE 3.1

ℓ	1	2	3	4	5	6	7	8	9	10	11	12
$Rs_{crit}(\ell)$	296	759	1702	3329	5869	9583	14759	21715	30792	42353	56809	71577

If $Rs < Rs_{crit}(1)$ then the velocity decays and the mean temper-

ature remains unchanged. (We have not found a numerical exam-

ple of sub-critical, finite-amplitude convection). The initial

growth rate of each eigenmode increases with increasing Rs as do

the ℓ-values of the most unstable modes.

For example, $\ell=6$ is the most unstable eigenmode for

$Rs = 10^8$. Although $\tilde{T}$ and ω grow rapidly, $<T>$ changes very slowly

and its growth rate is determined by the conductive timescale,

which is $\sim 10^{-5}$ of the growth rates of $\tilde{T}$ and ω for $Rs = 10^8$. The

horizontally averaged temperature does not begin to change appre-

ciably until the convective flux, $<\tilde{T}v_r>$, is of the same order as

the steady-state flux, $\mathcal{L}/r^2$. The mean temperature gradient

then becomes nearly isothermal (isothermal $\equiv$ adiabatic for a

Boussinesq fluid). At this point, the velocity is large and

chiefly made up of the most unstable eigenmodes (large ℓ) of

the conductive temperature gradient. The nearly isothermal tem-
perature gradient is not in equilibrium with a velocity field
with these characteristics. For steady-state equilibrium with a
nearly isothermal temperature gradient, the velocity must be made
up of the neutrally stable eigenmodes of that same temperature gra-
dient (not the conductive gradient). The latter eigenmodes are
characterized by smaller values of ℓ than the unstable eigen-
modes of the conductive gradient. Therefore the velocity begins
cycles of decay
and growth, with lower and lower values of ℓ dominating the velo-
city until a statistically steady-state is reached. The integra-
tion of the velocity forward in time is limited by a Courant con-
dition; a large velocity requires a small time-step. Because the
time-step must be small and because the velocity and temperature
must cycle through many stages until they reach a statistically
steady state, finding solutions by integrating equations (2.9) -
(2.15) forward in time is inefficient.

B. The Initial-Value Problem in Artificial Time

Instead of integrating the equations of motion in real time,
we can force the fluid to go through a series of states in which
the mean temperature gradient is always in instantaneous equili-
brium with the velocity field and convective flux. The only modi-
fication to the equations of motion (2.9) - (2.15) is to set
$\partial\langle T\rangle/\partial t = 0$ or equivalently to replace equation (2.15) with

$$
\frac{\partial \langle T\rangle}{\partial r} = - \mathcal{L}(r) / r^2 \\
+ \sum_{\gamma,\ell,m} T_{\gamma,\ell,m}\, \omega_{\gamma,\ell,m}\, \ell(\ell+1) / r
\tag{3.2}
$$

With this modified set of equations, $\tilde{T}$, $\tilde{\omega}$ and $\partial<T>/\partial r$ all initially grow exponentially. Within a few eddy-turnover times the solution converges to a statistically steady state. Any solution to the artificial time equations (2.9) - (2.14) and (3.2) in which $\partial<T>/\partial r$ does not change in time is also an exact equilibrium solution to the real time equations although it is not necessarily a stable solution. Stability is tested by adding a perturbation to the equilibrium solution, integrating it forward in real time, and testing to see whether the perturbations grow or decay. Regardless of the amplitude of the perturbation, we have never found a time-independent solution generated from the artificial time equations that was unstable in real time.

Sometimes the artificial time equations do not converge to a steady state but only to a statistically steady state (in which the mean temperature gradient, heat flux and spectra of the kinetic energy and thermal fluctuations are stationary). In these cases the variations in time of $\partial<T>/\partial r$ are small but they do not have the same time dependence that $\partial<T>/\partial r$ has in real time (see, Marcus 1980). If the statistically steady artificial time solutions are used as the initial data in integrating the equations in real time, the solution converges to a new statistically steady state in only a few eddy-turnover times.

IV. DESCRIPTION OF THE FLOW

In our modal representation of the fluctuating quantities, we have chosen $\ell_{cutoff} = 12$, which requires 168 modes, (γ, ℓ, m). By using a radial grid of 128 zones, each scalar is represented

by 21,50⁴ numbers. It therefore becomes important to decide which
quantities should be calculated to describe the flow in a sensible
manner.

A. The Temperature Gradient and Mean Thermal Energy

The rate of change of the mean thermal energy of the fluid
is determined by integrating equation (2.15) twice over the en-
tire radius of the sphere:

$$\partial [\int <T> \, dr^3] / \partial t = 4\pi \int_0^1 <H> \, r^2 \, dr + 4\pi \frac{\partial <T>}{\partial r} \Big|_{r=1} \qquad (4.1)$$

The first term on the right-hand side of equation (4.1) is the
rate at which energy is pumped into the fluid from the heat source;
the second term is the rate at which energy is conducted away
from the surface of the sphere. If the integration of equation
(2.15) is left as an indefinite integral, we obtain the equation
for the mean thermal heat flux:

$$- \partial <T>/\partial r + r^{-1} \sum_{\gamma,\ell,m} T_{\gamma,\ell,m} \, \omega_{\gamma,\ell,m} \, \ell(\ell+1) + \mathcal{L}(r)/r^2$$

$$= -r^{-2} \, \partial (\int_0^r dr' r'^2 <T>)/\partial t \qquad (4.2)$$

The first term on the left-hand side of equation (4.2) is the con-
ductive heat flux, and it is therefore important for us to com-
pute the mean temperature gradient. The second term on the left-
hand side of equation (4.2) is the convective flux F_{con}. Each
mode, (γ,ℓ,m), contributes to the flux with no cross terms be-

tween modes. We will find it useful to consider the convective flux carried by all modes with a particular value of ℓ, $F_{con}(\ell)$:

$$F_{con}(\ell) = r^{-1} \ell(\ell+1) \sum_{\gamma,m} \omega_{\gamma,\ell,m} \; T_{\gamma,\ell,m} \qquad (4.3)$$

with

$$F_{con} = \sum_{\ell} F_{con}(\ell) \qquad (4.4)$$

The third term on the left-hand side of equation (4.2) is the heat flux of the steady-state fluid. The right-hand side of equation (4.2) is the rate at which the stored thermal energy is being released.

B. Energy Spectra in 2 and 3 Dimensions

The kinetic energy per unit mass in a shell of radius r is (see Paper I):

$$KE(r) = \sum_{\ell} KE(\ell,r) \qquad (4.5)$$

with

$$KE(\ell,r) = \frac{1}{2} \ell(\ell+1) \sum_{\ell,m} \{\omega^2_{\gamma,\ell,m} \, \ell(\ell+1)$$

$$+ [\partial(r\omega_{\gamma,\ell,m})/\partial r]^2\}/r^2 + \psi^2_{\gamma,\ell,m} \qquad (4.6)$$

where $KE(\ell,r)$ is the kinetic energy due to all modes, (γ,ℓ,m) for, all γ and m. Similiarly we can define a fluctuating thermal energy[1]:

$$TE(r) \equiv 1/2 \; <\tilde{T}{}^2> = \sum_{\ell} TE(\ell,r) \qquad (4.7)$$

[1]TE(r) is usually called the temperature variance, but we reserve the term "variance" for another quantity.

with

$$TE\ (\ell,r) = 1/2 \sum_{\ell,m} \tilde{T}{}^{2}_{\gamma,\ell,m} \qquad (4.8)$$

Traditionally one calculates the fluctuating thermal energy and the kinetic energy spectra as functions of a 3-dimensional wave number, whereas $TE(\ell,r)$ and $KE(\ell,r)$ are functions of radius and the 2-dimensional wave number, ℓ. In a bounded spherical geometry it is more natural to compute these 2-dimensional spectra. Three-dimensional spectra are better suited to an unbounded or periodic Cartesian geometry. However, to compare our results with other published work, it is necessary to transform our 2-dimensional spectra into 3-dimensional spectra. Unfortunately, it is not a unique transformation. We provide an example with the thermal energy spectrum.

The correlation of the temperature is defined:

$$C(\underline{r}) = 1/2 \int \tilde{T}(\underline{x})\ \tilde{T}\ (\underline{x} + \underline{r})\ d^{3}x \qquad (4.9)$$

The integral is over all space, but because $\tilde{T}(\underline{x})$ is defined only for $|x| \leq 1$, it is necessary to insert a window function, $W(\underline{x},\underline{r})$, into the integral in equation (4.9). The simplest choice for $W(\underline{x},\underline{r})$ is

$$W(\underline{x},r) = \begin{cases} 1 & \text{if } |x| \leq 1 \text{ and } |\underline{x}+\underline{r}| \leq 1 \\ 0 & \text{otherwise} \end{cases} \qquad (4.10)$$

There are several problems with this definition of the window function. If $\tilde{T}$ were independent of position we would expect the correlation function to be independent of $\underline{r}$. Using equation

(4.10) we find that $C(\underline{r})$ decreases with increasing $|r|$. The decrease is due to the finite geometry and not due to an inherent property of $\tilde{T}$. The window function must be chosen to compensate for this effect. Another consideration in the choice of $W(\underline{x},\underline{r})$ is that our integrations are numerical and $\tilde{T}$ is represented on a radial grid with a truncated expansion in θ and ϕ. $W(\underline{x},\underline{r})$ must be chosen so that $C(r)$ reflects the properties of $\tilde{T}$ and not the numerical representation of $\tilde{T}$.

It is convenient to have $W(\underline{x},\underline{r}=0) = 1$ so that

$$C(0) = 4\pi \int_0^1 TE(r) \, r^2 dr \tag{4.11}$$

We define $\mathcal{C}(\underline{k})$ to be the Fourier tranform of $C(\underline{r})$

$$\mathcal{C}(\underline{k}) = (2\pi)^{-3} \int C(\underline{r}) \, \exp(-i\underline{k}\cdot\underline{r}) \, d^3r \tag{4.12}$$

Integrating $(\mathcal{C})$ over all directions, we obtain the 3-dimensional thermal energy spectrum that is a function of $k \equiv |\underline{k}|$.

$$TE(k) = (2\pi)^{-2} \int d\Omega_r dr \, dx^3 \tilde{T}(\underline{x}) \tilde{T}(\underline{x}+\underline{r}) \, \sin(kr) \, W(\underline{x},\underline{r}) \tag{4.13}$$

By choosing $W(\underline{x},\underline{r}=0) = 1$ we find that the integral of $TE(k)$ over all k is equal to the total fluctuating thermal energy.

$$\int_0^\infty TE(k) dk = 4\pi \int_0^1 TE(r) \, r^2 \, dr \tag{4.14}$$

If $W(\underline{x},\underline{r}) \equiv 1$, then $TE(k)$ reduces to

$$TE(k) = 1/2 \, (2\pi)^3 \int \tilde{T}_k \tilde{T}_{-k} \, k^2 \, d\Omega_k \tag{4.15}$$

where T_k is the Fourier transform of $\tilde{T}$. One final caution: since the spatial resolution is more limited in the horizontal

than in the radial direction, and since the horizontal res-
olution is $\sim 2\pi \, [\ell_{cutoff}(\ell_{cutoff}+1)]^{-1/2}$, we should not expect TE(k)
to be accurate for $k > [\ell_{cutoff}(\ell_{cutoff}+1)]^{1/2}$. Similiarly TE(k)
will not be accurate for $k < 1$.

C. 3-Dimensional Energy Spectrum in Terms of Modes

In terms of modes, equation (4.13) becomes

$$TE(k) = (2\pi)^{-1}\int d\Omega_x \, d\Omega_r \, dr \, dx \, x^2 \, kr \, \sin(kr) \, W(\underline{x},\underline{r})$$

$$\left[\left[\sum_\ell \left\{ \sum_{m\geq 1} [T_{R,\ell,m}(x) - iT_{I,\ell,m}(x)] \, Y^{\ell,m}(\Theta_x,\phi_x)\right.\right.\right.$$

$$+ [T_{R,\ell,m}(x) + i\,T_{I,\ell,m}(x)] \, (-1)^m \, Y^{\ell,-m}(\Theta_x,\phi_x)$$

$$\left.+ 2^{1/2} \, T_{R,\ell,o}(x) \, Y^{\ell,o}(\Theta_x,\phi_x)\right\}\right]\right]$$

$$\times \sum_{\ell'} \left\{ \sum_{m'\geq 1} [T_{R,\ell',m'}(|\underline{x}+\underline{r}|) - iT_{I,\ell',m'}(|\underline{x}+\underline{r}|)]Y^{\ell',m'}(\Theta_{x+r},\phi_{x+r})\right.$$

$$+ \, [T_{R,\ell',m'}(|\underline{x}+\underline{r}|) + iT_{I,\ell',m'}(|\underline{x}+\underline{r}|)](-1)^{m'}Y^{\ell',m'}(\Theta_{x+r},\phi_{x+r})\right\}$$

$$\left.+ 2^{1/2} \, T_{R,\ell',o}(|x+r|) \, Y^{\ell',o}(\Theta_{x+r},\phi_{x+r})\right] \qquad (4.16)$$

The spherical coordinates of the vector $(\underline{x}+\underline{r})$ are Θ_{x+r} and ϕ_{x+r}.
We have chosen the z-axis of the (Θ_r,ϕ_r) coordinate system to be
the Θ_x axis. Using the identity

$$\int Y^{\ell,m}(\Theta_x,\phi_x) \, Y^{\ell',-m'}(\Theta_{x+r},\phi_{x+r}) \, d\Omega_x \, d\Omega_r$$

$$= 2\pi \, P_\ell \, [\cos(\Theta_{x+r})] \, \delta_{\ell\ell'} \quad \delta_{mm'} \qquad (4.17)$$

and assuming that W depends only on $|\underline{x}|$, $|\underline{r}|$ and the angle be-
tween $\underline{x}$ and $(\underline{x}+\underline{r})$, we find that the fluctuating thermal energy

spectrum is

$$TE(k) = 2\int d(\cos\Theta_r)\, dr\, dx\, x^2\, kr\, \sin(kr)$$

$$\times\, W(x,r,\theta_{r+x})$$

$$\times\, \sum_{\gamma,\ell,m}\, [T_{\gamma,\ell,m}(x)\, T_{\gamma,\ell,m}\,(|\underline{x}+\underline{r}|)\, P_\ell(\cos\Theta_{x+r}) \tag{4.18}$$

In equations (4.17) and (4.18), $P_\ell(\cos\Theta_{x+r})$ is a Legendre polynomial, and

$$\cos(\Theta_{x+r}) = (\underline{x}^2 + |\underline{x}+\underline{r}|^2 - \underline{r}^2)\,/\,(2x|\underline{r}+\underline{x}|) \tag{4.19}$$

$$|\underline{x}+\underline{r}| = (\underline{x}^2 + \underline{r}^2 + 2\underline{r}\,\underline{x}\cos\Theta_r)^{1/2} \tag{4.20}$$

Not suprisingly, equation (4.18) shows that TE(k) depends upon the product of $T_{\gamma,\ell,m}(|\underline{x}|)$ and $T_{\gamma,\ell,m}(|\underline{x}+\underline{r}|)$, but contains no cross terms between different modes.

When the flow is isotropic the 3-dimensional spectrum can be directly related to the 2-dimensional spectrum. If the correlation $C(\underline{\tilde{r}})$ between $T(\underline{x})$ and $T(\underline{\tilde{x}+r})$ depends only on $|r|$ and if W depends only on $|x|$ and $|r|$ then equation (4.18) reduces to

$$TE(k) = (2/\pi)\int dr\, dx\, x^2\, kr\, \sin(kr)$$

$$\times\, W(x,r)$$

$$\times\, \sum_{\gamma,\ell,m}[T_{\gamma,\ell,m}(x)]^2\quad P_\ell\,(1 - 1/2\, r^2/x^2) \tag{4.21}$$

Defining

$$d_\ell(kx) \equiv (4/\pi) \int_0^{2xk} y \sin(y) \; P_\ell(1 - 1/2 \; y^2/k^2x^2)dy \qquad (4.22)$$

we find that

$$TE(k) = k^{-1} \sum_\ell r^2 TE(\ell,r) \; d_\ell(kr) \; dr \qquad (4.23)$$

D. Total Energy Budgets

Multiplying the Boussinesq Navier-Stokes equation by the velocity and integrating over the volume we obtain the kinetic energy budget:

$$\partial \; [1/2 \int dr^3 v^2]/\partial t = 4\pi P_r R_s \int_0^1 <v_r T> \; r^3 dr$$
$$- P_r \int dr^3 \; (\frac{\partial v_i}{\partial x_j})(\frac{\partial v_i}{\partial x_j}) \qquad (4.24)$$

where the first term on the right-hand side of equation (4.24) is KE_{in}, the total rate at which kinetic energy is pumped into the fluid from buoyancy forces, and the second term on the right-hand side is KE_{out}, a negative-definite quantity that is the rate at which viscosity dissipates the kinetic energy. If the convective flux is much greater than the conductive flux and if the time variation of $<T>$ is slow enough such that

$$<TV_r> \; \simeq \; \mathcal{L}/r^2 \qquad (4.25)$$

then

$$\mathcal{L}(r) \gg |\partial(\int_0^r dr'r'^2<T>)/\partial t| \qquad (4.26)$$

and

$$KE_{in} \approx 4\pi P_r R_s \int_0^1 \mathcal{L}(r)r \; dr = 1.892 \; \pi P_r R_s \tag{4.27}$$

In dimensionless units the rate at which mean thermal energy is generated is unity. From equation (4.27) it is apparent that in Boussinesq fluids the rate at which kinetic energy is created is much greater than the rate at which the mean thermal energy is created. This conclusion is quite different from the one derived from mixing-length arguments in a compressible fluid. In a compressible fluid these two energy input rates are nearly the same. It is because a Boussinesq fluid is incompressible (and can perform no mechanical work) that the mean thermal energy generation rate and kinetic energy generation rate are not equi-partitioned.

It is often assumed that the rate at which kinetic energy enters the fluid is approximately equal to V_{big}^3/L_{big} where V_{big} and L_{big} are the characteristic velocity and length of the largest convective eddies. Equating this expression for KE_{in} with equation (4.27) we obtain

$$V_{big} \approx (P_r R_s)^{1/3} \tag{4.28}$$

This provides a scaling law for V_{big} that can be numerically verified. Furthermore, if most of the convective flux is transported by the largest convective eddy (with characteristic temperature fluctuation $\sim T_{big}$), then

$$\langle \tilde{T}_{big} \; V_{big} \rangle \approx \mathcal{L}/r^2 \approx 1 \tag{4.29}$$

and

$$T_{big} \simeq (P_r R_s)^{-1/3} \tag{4.30}$$

Equation (4.28) can also be verified numerically.

By multiplying the thermal diffusion equation by $\tilde{T}$ and integrating over the volume, we obtain the fluctuating thermal energy budget

$$\partial \left[1/2 \int <\tilde{T}{}^2> dr^3 \right] = -4\pi \int_0^1 <\tilde{T} v_r> \frac{\partial <T>}{\partial r} r^2 dr$$

$$- 4\pi \int_0^1 <\overset{\sim}{\nabla T} \cdot \overset{\sim}{\nabla T}> r^2 dr \tag{4.31}$$

The first term on the right-hand side of equation (4.31) is TE_{in}, the rate at which fluctuating thermal energy is created from the interaction of the mean temperature gradient with the convective flux. The second term on the right-hand side of equation (4.29) is TE_{out}, a negative definite quantity that is the rate of diffusion of the thermal energy.

E. Detailed Energy Budgets for Each ℓ-Value

Each shell of modes with the same horizontal wavelength [i.e., all modes (γ, ℓ, m) with the same value of ℓ] has an inflow and outflow of kinetic and fluctuating thermal energy. It is useful to determine the rate at which energy is dissipated and created in each particular ℓ-shell. The rate of change of the kinetic energy in the ℓth shell is

$$\partial \left(4\pi \int_0^1 KE(r, \ell) r^2 dr \right)/\partial t = KE_{in}(\ell) - KE_{out}(\ell)$$

$$- 4\pi \int_0^1 <\underline{v}(r, \ell) \cdot [(\underline{v} \cdot \nabla) \underline{v}]> r^2 dr \tag{4.32}$$

where $KE_{in}(\ell)$ is equal to the rate at which kinetic energy is directly fed into the ℓth shell

$$KE_{in}(\ell) = 4\pi \, P_r R_s \sum_{\gamma,m} \ell(\ell+1) \int_0^1 \omega_{\gamma,\ell,m} T_{\gamma,\ell,m} r^2 dr \qquad (4.33)$$

and where $KE_{out}(\ell)$ is the rate at which the ℓth shell directly loses kinetic energy through viscous dissipation

$$KE_{out}(\ell) = -4\pi \, P_r \int_0^1 \left[\!\left[r^{-1}\partial^2[rKE(\ell,r)/\partial r^2 \right.\right. \qquad (4.34)$$
$$+ \sum_{\gamma,m} \{-[\ell(\ell+1)]^2 \, r^{-2} \, \omega_{\gamma,\ell,m} \, \mathcal{D}_\ell \, (\omega_{\gamma,\ell,m})$$
$$-\ell(\ell+1) \, r^{-2} \, \partial(r\omega_{\gamma,\ell,m})/\partial r \; \partial[r \, \mathcal{D}_\ell \, (\omega_{\gamma,\ell,m})]/\partial r$$
$$\left.\left. - \, \ell(\ell+1) \, \psi_{\gamma,\ell,m} \, \mathcal{D}_\ell \, (\psi_{\gamma,\ell,m})\} \right]\!\right] r^2 dr$$

In equation (4.32), $\underline{v}(r,\ell)$ is the velocity associated with the ℓth shell at radius r. If the flow is stationary the left hand side of equation (4.32) is zero, but $\langle\langle KE_{in}(\ell)\rangle\rangle \neq \langle\langle KE_{out}(\ell)\rangle\rangle$ because $-4\pi \int \langle \underline{v}(r,\ell)\cdot[(\underline{v}\cdot\nabla)\underline{v}] \rangle \, r^2 dr$, which is the rate at which kinetic energy cascades in or out of the ℓth shell from other shells, is not necessarily zero. By comparing the relative values of $KE_{in}(\ell)$, $KE_{out}(\ell)$, and $-4\pi \int \langle \underline{v}(r,\ell)\cdot[(\underline{v}\cdot\nabla)\underline{v}] \rangle \, r^2 dr$, we can determine whether an ℓ-shell is part of the production, dissipation, or equilibrium range of the spectrum.

The rate of change of fluctuating thermal energy in the ℓth shell is given by

$$\partial[4\pi \int_0^1 TE(r,\ell) \, r^2 dr]/\partial t = TE_{in}(\ell) - TE_{out}(\ell)$$
$$- 4\pi \int_0^1 \langle T(\ell,r) \, [(\underline{v}\cdot\nabla) \, \tilde{T}] \rangle \, r^2 dr \qquad (4.35)$$

The rate of fluctuating thermal energy input, $TE_{in}(\ell)$, is

$$TE_{in}(\ell) = -4\pi \int_0^1 \frac{\partial \langle T \rangle}{\partial r} r \sum_{\gamma,m} T_{\gamma,\ell,m} \, \omega_{\gamma,\ell,m} \, \ell(\ell+1) \, dr \qquad (4.36)$$

and the rate of fluctuating thermal energy dissipation is

$$TE_{out}(\ell) = -4\pi \sum_{\gamma,m} [(\partial T_{\gamma,\ell,m}/\partial r)^2 + \ell(\ell+1) r^{-2} T^2_{\gamma,\ell,m}] \, r^2 \, dr \qquad (4.37)$$

The rate at which fluctuating thermal energy cascades in or out of the ℓth shell from neighboring shells is $-4\pi \int_0^1 T(\ell,r) [(\underset{\sim}{v} \cdot \nabla) \tilde{T}] \, r^2 \, dr$, where $T(\ell,r)$ is the thermal fluctuation of the ℓth shell at radius r.

F. Vorticity, Isotropy, and Angular Momentum

The vorticity, $\mathcal{R}$ is solenoidal and can be expressed in terms of modes as

$$\mathcal{R} = \nabla[\partial(r\psi)/\partial r] - (r\nabla^2 \psi) \, \hat{e}_r - r\nabla [(\nabla^2 \omega) \, \hat{e}_r] \qquad (4.38)$$

One possible test for the isotropy of the velocity is to compute the helicity, $\langle \mathcal{R} \cdot \underline{v} \rangle$, which is zero for an isotropic field. In terms of modes, the helicity is given by

$$\langle \underline{v} \cdot \mathcal{R} \rangle = \ell(\ell+1) \, r^{-2} \sum_{\gamma,\ell,m} 2\ell(\ell+1) \, \omega_{\gamma,\ell,m} \, \psi_{\gamma,\ell,m}$$

$$+ \; \partial(r\omega_{\gamma,\ell,m})/\partial r \; \partial(r\psi_{\gamma,\ell,m})/\partial r$$

$$- \; r\psi_{\gamma,\ell,m} \; \partial^2(r\omega_{\gamma,\ell,m})/\partial r^2 \qquad (4.39)$$

From equation (4.39) it is clear that the helicity is made up of terms that are proportional to $\psi_{\gamma,\ell,m}\omega_{\gamma,\ell,m}$ and its derivatives. We normally expect that the poloidal part of the velocity is domi-

nated by the low ℓ modes, whereas the toroidal component of the velocity (as well as the vorticity itself) is dominated by the high ℓ modes. Therefore the helicity is less a test of isotropy than a measure of the correlation between the large scale and small structure of the velocity. In a calculation where the large scale communicates with the small scale by a series of cascades (each of which introduces its own phase shifts) the helicity is not a useful measure of isotropy. Instead, we shall use a less rigorous but more straightforward and revealing method to determine the anisotropy of the velocity. We define an isotropy function, $I(\ell,r)$ as a function of r for each ℓ-shell to be

$$I(\ell,r) \equiv 1/2 \ KE_H \ (\ell,r)/KE_R(\ell,r) \tag{4.40}$$

where $KE_R(\ell,r)$ and $KE_H(\ell,r)$ are the contributions to the kinetic energy, $KE(\ell,r)$, that are due respectively to the radial and horizontal components of the velocity. If $I(\ell,r)=1$, the flow is defined as isotropic. There are several advantages in defining a measure of isotropy as a function of both ℓ and r. First of all, convection is not by nature isotropic; the buoyancy force is in the radial direction, so we expect the radial component of the velocity to dominate. We expect that $I(\ell,r)$ will be less than 1 when ℓ is part of the production range. For larger ℓ-shells we expect that the velocity field will no longer feel the direct effect of the radial buoyancy; as the energy cascades downward the velocity should lose its memory of the radial direction and become more isotropic. This return to isotropy can be tested by determining whether $I(\ell,r)$ increases with increasing ℓ. We

also expect $I(\ell,r)$ to vary with the radius. At the outer boundary of
the sphere, the radial component of the velocity goes to zero.
The outer boundary-layer should be characterized by large values
of $I(\ell,r)$. We determine the behavior of $I(\ell,r)$ by expressing it
in terms of modes:

$$I(\ell,r) \equiv \sum_{\gamma,m} \ell(\ell+1)\, \omega^2_{\gamma,\ell,m} \Big/$$

$$\sum_{\gamma,m} \{[\partial(r\omega_{\gamma,\ell,m})/\partial r]^2 + r^2 \psi^2_{\gamma,\ell,m}\} \tag{4.41}$$

By using the regularity conditions at the origin, equation (4.41)
shows that

$$\lim_{r \to 0} I(\ell,r) \to 1 \qquad \text{for all } \ell \tag{4.42}$$

Equation (4.42) is due to the singularity of the coordinate sys-
tem at the origin (i.e. there is no distinction between radial and
horizontal), so $I(\ell,r)$ is not a useful measure of isotropy at the
origin. (However, at the origin $I(\ell,r)$ is the ratio of two
small, numerically computed quantities. By comparing it to its
known analytic behavior at the origin, it provides us with a use-
ful test of the accuracy of our numerical code.)

One more useful quantity to compute is the distribution of
angular momentum in the fluid. All of the angular momentum re-
sides in the $\ell = 1$ toroidal modes. Defining $\underline{j}(r)$ to be the
angular momentum per unit mass at radius r we find (Paper I):

$$\underline{j}(r) = 2(3)^{-1/2} r \left(\psi_{R,1,o} \, \hat{e}_z - \psi_{R,1,o} \, \hat{e}_x - \psi_{I,1,1} \, \hat{e}_y \right) \quad (4.42)$$

V. RESULTS OF NUMERICAL CALCULATIONS FOR RAYLEIGH NUMBER = 10^4 AND PRANDTL NUMBER = 10

A. Convergence to a Unique Stable, Equilibrium Solution

We have integrated the artificial and real time equations for $Rs = 10^4 (\sim 33.8 \, Rs_{crit})$ and $Pr = 10$, using a code that is second-order accurate in both space and time. The solution to the artificial time equations was found to be time-independent. This solution, plus a perturbation, was used as the initial data in the real time equations. The perturbation decayed, and the solution reconverged to the steady-state solution of the artificial time equations. We performed the integration several times: we used a radial grid that varied between 64 and 128 zones, an ℓ_{cutoff} in the Galerkin truncation that varied between 6 and 12, several different time-steps, and a large number of different initial conditions to the artificial and real time equations. (All of the initial conditions had total angular momentum equal to zero.) In each case the integrations converged to the same time-independent solution. (When ℓ_{cutoff} was less than 12 we found that the small ℓ modes did not change, but there was some change in the modes with ℓ near ℓ_{cutoff}. (See §5c.)

The final, stable solution has two orthogonal planes of reflection symmetry. Despite our attempts to introduce perturbations without this symmetry, the solution stubbornly remained reflection symmetric. Modes with other symmetries, such as dodecahedral modes, were found to be unstable.

A solution that is reflection symmetric with respect to both the x=o plane and z=o plane can be written so that ω and T are made up only of (R,ℓ=even,m=even) and (I,ℓ=odd,m=odd) modes and ψ made up only of (R,ℓ=even,m=odd) and (I,ℓ=odd,m=even) modes. However, in no case did the planes of symmetry coincide with the x=o, y=o, or z=o planes; therefore, <u>all</u> modes are present in our final solutions. In fact, different initial conditions always lead to different final values of $\omega_{\gamma,\ell,m}$, $\psi_{\gamma,\ell,m}$, $T_{\gamma,\ell,m}$, $P_{\gamma,\ell,m}$ and $\phi_{\gamma,\ell,m}$ because the planes of symmetry always lie in different directions. We consider it an excellent test of our numerical code (especially the cumbersome nonlinear terms) that all of the different initial conditions lead to solutions with different planes of symmetry and that the solutions are identical when they are rotated such that their planes of symmetry coincided with the x=o and y=o planes.

Notice that a solution with 2 orthogonal planes of reflection symmetry has its angular momentum identically equal to zero in all of its radial shells; if the solution is oriented such that the planes of reflection lie in the x=o planes, then $\psi_{R,\ell=1,m=1}$ = $\psi_{R,\ell=\phi,m=0}$ = $\psi_{I,\ell=1,m=1}$=o, therefore $\underline{j}$(r)=o for all r. Conservation of angular momentum requires only the integral constraint $\int_{o}^{1}$ (r)r^2 dr=0. The system was not constrained to have j(r)=0 for all r. We also note that although the ℓ=1 component of the toroidal component of the velocity vanishes identically, the toroidal velocity is about one-tenth the poloidal velocity for ℓ=2.

B. Temperature Gradient and Heat Flux

The mean temperature gradient of the steady-state convective solution is shown in Figure 1 (solid line) along with the temperature gradient of the conductive solution (dotted line). The convective gradient is, of course, more isothermal than the conductive solution, but it still shows a cusp at $r = 0.3$, which is the boundary of the internal heat source. Apparently the convective velocity and temperature fluctuations are sufficiently local that the convective flux cannot completely smooth out the cusp at $r = 0.3$. Because the convective solution is steady state, $1/r\ \partial<T>/\partial r$ must be equal to -1 at the outer boundary. The slope of $1/r\ \partial<T>/\partial r$ must be equal to zero at the origin. The temperature gradient is positive between $r = 0.55$ and $r = 0.86$, which means that the convective flux is so large that the conductive flux is negative in this region. A negative conductive flux is a familiar property of convection in plane-parallel geometries (Herring, 1963). Figure 2 shows the ratio, F_{con}/F_{Total}, where F_{Total} is the total flux and is equal to $\mathcal{L}(r)/r^2$ in steady-state convection. The ratio F_{con}/F_{Total} is the ratio of heat flux that is carried by convection to the total heat flux. The ratio is near unity over most of the radius of the sphere except in the outer boundary layer where it must go to zero. In §4 it was shown that the slope of F_{con}/F_{Total} goes to zero at the origin (unless the

leading order terms of $\omega_{\gamma,\ell=1,m}$ or $\tilde{T}_{\gamma,\ell=1,m}$ vanish at the origin). The mean temperature as a function of radius (Figure 3) prominently shows a "footprint" of the $r = 0.3$ boundary. Boundary conditions necessitate that $<T(1)>$ is zero for both the convective and conductive solution, but the value of $<T>$ at the origin can change. In conductive equilibrium $<T(0)> = 4.0$, whereas in convective equilibrium $<T(0)> = 0.68$.

C. Energy Spectra

The 2-dimensional spectra of the kinetic and fluctuating thermal energies evaluated at $r = 0.5$ are shown in figures 4 and 5. Both curves clearly exhibit the exponential decay that is characteristic of a dissipation spectrum. The total rate at which kinetic energy is dissipated from the fluid, KE_{out} is determined from equation (4.22) and is found to be 4.96×10^5. The Kolmagorov length-scale, η, is defined (Tennekes and Lumley, 1972)

$$\eta \equiv (P_r^3 \,/\, <<KE_{out}>>)^{1/4} \qquad (5.1)$$

and is equal to 0.212 in dimensionless units.

The equivalent thermal length-scale, η_θ, for which thermal diffusion becomes overwhelming is defined as

$$\eta_\theta = P_r^{-1/2} \, \eta \qquad (5.2)$$

and is equal to .067. With 128 grid points and $\ell_{cutoff} = 12$ both of these scales should be numerically resolvable. Because η is greater than η_θ, we expect the dissipation part of the kinetic energy spectrum to extend to lower values of ℓ than

in   the fluctuating temperature spectrum. Nearly the entire
kinetic energy spectrum is exponential while   TE(ℓ, r=0.5) is
fairly flat for $\ell \lesssim 3$. This flatness is
due to the combined effects of production, cascade and dissipa-
tion. Because all of the effects are squeezed into a short range
of the spectrum, there is no clearly identificable production or con-
vective-viscous subrange. For $\ell > 3$, TE(ℓ,r) is dominated by dis-
sipation.

Both TE(ℓ,r) and KE(ℓ,r) curl upward at the high ℓ end of
the spectrum. This is a typical phenomena of a Galerkin trunca-
tion and is due to the fact that energy can cascade down the spec-
trum until it reaches ℓ_{cutoff}. At ℓ_{cutoff} the energy can cascade
no further, so the velocity at ℓ_{cutoff} is forced to increase until
$KE_{out}(\ell_{cutoff})$ is large enough to dissipate all of the
accumulated energy.   The fact that TE(ℓ,r) curls up more
than KE(ℓ,r) is due to the fact that Pr > 1. Most of the kinetic
energy can dissipate before cascading into ℓ_{cutoff}. However, the
fluctuating thermal energy is not dissipated as efficiently, so more
cascades down to ℓ_{cutoff} before being dissipated, resulting in a
greater curl. We have shown that the upward
curl   at ℓ_{cutoff} is a truncation effect by repeating the cal-
culation with ℓ_{cutoff} = 10. In the latter calculation the spec-
tra curl at ℓ = 10 while with ℓ_{cutoff} = 12 there was no curl
at ℓ = 10. If the integration is performed with a Prandtl
number of 0.1, KE(ℓ,r) curls up more than TE(ℓ,r).

It is because TE(ℓ,r) and KE(ℓ,r) both decay exponentially
at large ℓ that our modal truncation is valid. If we found that
KE(ℓ,r) or TE(ℓ,r) decayed slowly as a function of ℓ, the modal

truncation would not have been a good approximation.

We have computed the kinetic energy spectrum as a function of the 3-dimensional wave number, k. According to Corrsin (1964) the 3-dimensional dissipative kinetic energy spectrum should be of the form

$$KE(k) = \alpha\varepsilon^{2/3} k^{-5/3} \exp [-3\alpha(k\eta)^{4/3} 1/2] \qquad (5.3)$$

where α is a constant on the order of unity. Figure 6 shows our computed spectrum with $(k\eta)^{4/3}$ as the independent variable. Fitting the slope of the curve in figure 6 to equation (5.3) between $k=4$ and $k=8$, we have determined α to be 3.07. While we should be somewhat cautious in our interpretation of our deconvolved 3-dimensional spectrum (see §4b), it is interesting to note that our computed values of log $[KE(k)]$ are proportional to $k^{4/3}$ and not k.

Since both $TE(\ell,r)$ and $KE(\ell,r)$ decay exponentially with ℓ, it is not surprising that the convective flux, $\sim F_{con}(\ell)$, carried by the ℓth shell of modes, decreases with ℓ. Figure 7 shows the fraction of the convective flux carried by the ℓth shell at $r = 0.5$. Nearly 90% of the convective flux is carried by the $\ell=1$ modes. We conclude that the amount of flux we have neglected by truncating at $\ell=12$ is negligible.

D. Energy Balance

In figure 8 we have plotted $TE_{in}(\ell)/TE_{in}$ and $KE_{in}(\ell)/KE_{in}$ which are, respectively, the fractions of thermal and kinetic energy that each ℓ-shell contributes to the fluid. These ratios both decrease rapidly as ℓ increases   with $\sim 93\%$ of KE_{in} and

$\sim 73\%$ of TE_{in} produced by the $\ell=1$ modes. Because the Prandtl number is greater than 1, $KE_{in}(\ell=1)/KE_{in}$ is greater than $TE_{in}(\ell=1)/TE_{in}$. Furthermore, $KE_{in}(\ell)/KE_{in}$ decreases faster than $TE_{in}(\ell)/TE_{in}$.

We have plotted the ratios $KE_{out}(\ell)/KE_{in}(\ell)$ and $TE_{out}(\ell)/TE_{in}(\ell)$ in figure 9. The ratio $KE_{out}(\ell)/KE_{in}(\ell)$ is equal to the rate at which kinetic energy is directly dissipated (not leaked through a cascade) from the ℓth shell divided by the rate at which kinetic energy directly enters the ℓth shell. We would expect this ratio to be small if ℓ were in a production range and large in the dissipative range. The fact that $KE_{out}(\ell)/KE_{in}(\ell)$ is approximately 1 for all ℓ can be interpreted in the following way: there is no (or very little) kinetic energy cascade, so the amount of kinetic energy that is generated in the ℓth shell is directly dissipated by the ℓth shell and not transferred to neighboring shells. This interpretation is supported by the fact that the computed nonlinear terms in the model Navier-Stokes equation (2.7) are much smaller than the viscous, pressure and buoyancy terms. The lack of nonlinear interaction is also shown by the fact that the poloidal velocity (which is directly fed by buoyancy) is much larger than the toroidal velocity, which is fed energy only through the nonlinear cascade. The values of $TE_{out}(\ell)/TE_{in}(\ell)$ plotted in figure 9 show that there is a thermal cascade. $TE_{out}(1)/TE_{in}(1)$ is less than 1 which means some of the fluctuating thermal energy in the $\ell=1$ shell must be cascading to higher values of ℓ. For $\ell \geq 2$, $TE_{out}(\ell)/TE_{in}(\ell)$ is larger than 1 which means these modes are dissipating more energy than they produce. The extra energy that these shells dissi-

pate is provided by their neighbors. The thermal cascade is plausible because the nonlinear terms of the thermal diffusion equation (2.9) are of the same order as the dissipative terms.

A test of the accuracy of our code is that it conserves energy; the computed values of KE_{out} and KE_{in} are 4.96×10^5 and 4.94×10^5 respectively. The computed values of TE_{out} and TE_{in} are 4.09 and 4.08.

E. Structure of the $\ell=1$ Modes

Because the $\ell=1$ modes dominate the flow, we illustrate the $\ell=1$ radial component of the velocity, $\ell(\ell+1) \, r^{-1} \, \omega_{I,1,1}$ in figure 10 and the temperature, $\tilde{T}_{I,1,1}$, in figure 11. The $\ell=1$ component of the toroidal velocity, ψ, is equal to zero for all r. For these two figures, we have rotated the planes of symmetry to coincide with the x=o and z=o plane. Figure 10 is normalized by the maximum value of the $\ell=1$ radial component of the velocity, $\max v_r^{\ell=1} = 33.8$. Notice that the velocity is a smooth function of radius and shows no cusp at r = 0.3. On the other hand, $\tilde{T}_{I,1,1}$ does show a strong peak at r = 0.3. Figure 11 is normalized by its maximum value, $\max T_{I,1,1}$ = 0.0226. It is interesting to compare the maximum value of $v_r^{\ell=1}$ with its estimated value of 46 derived from the scaling law (equation 4.28). The scaling law for the velocity is therefore fairly accurate for this flow. The Peclet number, in dimensionless units, is just equal to the velocity, so the Reynolds number is approximately equal to $\max v_r^{\ell=1}/P_r \approx 63$.

F. The 2-Dimensional Spectra and Boundary Layer Thickness

In figures 12 and 13 we have plotted $KE(\ell,r)/r^2$ and $TE(\ell,r)/r^2$ as functions of radius for all ℓ. All of the 24 graphs have been normalized by their maximum values. Except for $\ell=1$, $KE(\ell,r)/r^2$ is zero at the origin. As r increases, the curves remain near zero until they reach a critical value of radius and steeply rise to a peak. The critical value of r at which the curves begin to rise and the radius of the peak itself both increase with increasing values of ℓ. This behavior is consistent with the fact that $KE(\ell,r) \sim r^{2\ell}$ near the origin (Paper I). For $\ell \geq 2$, $KE(\ell,r)/r^2$ decreases after its peak to a local minimum and then sharply increases at $r = 1.0$. This is because most of the kinetic energy in the first peak is due to radial motions. As v_r goes to zero at $r = 1$, $KE(\ell,r)/r^2$ decreases. Very close to the outer boundary, the horizontal components of the velocity increase rapidly in order to conserve mass flux, and $KE(\ell,r)/r^2$ increases accordingly.

We define $X(\ell)$ to be the distance between $r = 1.0$ and the radius of the local minimum of $KE(\ell,r)/r^2$ and we use it as a measure of the boundary-layer thickness for each ℓ. Figure 12 shows that for $\ell \leq 6$, $X(\ell)$ slowly decreases with increasing ℓ, and remains at a nearly constant value for $\ell \geq 7$. The values of $X(\ell)$ were found to be insensitive to changes in the number of radial grid points or to stretching the grid near the boundary. We can understand the behavior of $X(\ell)$ by examining the energetics of the boundary-layer. The rate at which kinetic energy is dissipated from the boundary-layer associated with the ℓth shell is:

$$4\pi \, P_r \int_{1-X}^{1} \underline{v}(\ell,r) \cdot \nabla^2 \, \underline{v}(\ell,r) \, r^2 dr \approx 4\pi P_r \, v(\ell,r=1)^2/X \quad (5.4)$$

What is the rate at which kinetic energy enters the boundary-layer? For large values of ℓ, the amount of kinetic energy that enters the boundary-layer directly from the buoyancy forces is small compared to the rate at which kinetic energy is advected in. The rate of advection is proportional to the density of kinetic energy in the ℓth-shell multiplied by the surface area of the boundary layer ($\sim 4\pi$) multiplied by the largest characteristic velocity, V_{big}:

$$2\pi \, [v(\ell, \, r=1)]^2 \, V_{big} \quad (5.5)$$

Setting expressions (5.4) and (5.5) equal to each other, we see that $v(\ell, r=1)$ cancels and that $X(\ell)$ becomes independent of $v(\ell,r)$ and ℓ for large ℓ.

The thermal energy spectra, $TE(\ell,r)$, display some of the same properties that the kinetic energy spectra have. As ℓ increases, the radius at which the spectra rise and peak also increases. This is not surprising since both $TE(\ell,r)$ and $KE(\ell,r)$ behaves as $r^{2\ell}$ near the origin. Unlike the kinetic energy spectra, though, $TE(\ell,r)/r^2$ shows several peaks. For $TE(\ell=1,r)/r^2$ (the square of the function plotted in figure 11) a large peak occurs at the boundary of the heat source, $r = 0.3$, and a smaller peak occurs at $\sim r = 0.88$, the radius at which the convective flux (figure 2) drops to zero. These two peaks can be seen in $TE(\ell,r)/r^2$ for $\ell < 6$. At $\ell = 6$ the two peaks merge. Comparing figures 12 and 13 it is strikingly apparent that

$TE(\ell,r)/r^2$ has a more small scale structure than $KE(\ell,r)/r^2$. At first this structure was thought to be numerical. Testing shows that it is reproducible and independent of radial grid changes. One reason that the kinetic energy is smoother than the thermal energy spectrum is that the Prandtl number is greater than 1. Viscosity if better at smoothing the velocity than thermal diffusivity is at smoothing the temperature. As further evidence of the viscosity's smoothing effect, we have seen (figure 10) that the $\ell=1$ component of the velocity shows no evidence of the heat source, while the temperature shows a marked peak. The small scale radial structure in $T_{\gamma,\ell,m}$ is due to the temperature and momentum advection terms, $(\underline{v}\cdot\nabla T)_{\gamma,\ell,m}$ and $(\underline{v}\cdot\nabla\underline{v})_{\gamma,\ell,m}$ in the Boussinesq equations. Both of these nonlinear terms are a sum of many products of $T_{\gamma',\ell',m'}$, $\omega_{\gamma'',\ell'',m''}$ and $\psi_{\gamma''',\ell''',m'''}$. Since $T_{\gamma',\ell',m'}$, $\omega_{\gamma'',\ell'',m''}$ and $\psi_{\gamma''',\ell''',m'''}$ each peak at different radii, the advection terms and $T_{\gamma,\ell,m}$ can have small scale radial structure.

G. Isotropy

Our measure of isotropy, $I(\ell,r)$, is plotted in figures 14 and 15 for $\ell=1$ and $\ell=2$. Both curves have several grid points near $r=0$ and as r goes to zero, $I(\ell,r)$ smoothly approaches 1 which shows the numerical code is accurate near the origin (see §4f). Figure 14 shows that the horizontal component of the $\ell=1$ velocity goes to zero at $r=0.67$ and then rapidly increases in the outer boundary layer. The obvious conclusion to be drawn from $I(\ell=1,r)$ is that the large scale structure of the convective velocity is

markedly anisotropic.

We have illustrated $I(\ell=2,r)$ because it is very similar to all of the $I(\ell,r)$ curves with $\ell>1$. For $\ell>1$, $I(\ell,r)$ diminishes with increasing radius (although it never goes to zero) and then increases in the boundary-layer. Because $I(\ell>1,r)$ never goes to zero, we might argue that the velocity for modes with $\ell>1$ is more isotropic than the velocity when $\ell=1$. However, there is certainly no evidence for a "return to isotropy" in the small-scale modes. The lack of isotropy in the small scales is not surprising since there is not much of an energy cascade and the velocity (Reynolds number ≈ 3) is far from being turbulent.

DISCUSSION

We have computed the convective flow with a Prandtl number of 10 and with a Rayleigh number that is ~ 30 times the critical value. Despite a variety of initial 3-dimensional configurations of the flow, the fluid always evolves to the same steady-state with two orthogonal planes of reflection symmetry. This computation differs from previous studies of convection because the equations of motion have been used to determine the horizontal structure of the flow; an a priori horizontal structure was not imposed as a constraint to the equations of motion. We emphasize that to determine the stability of a convective solution, an examination of only the large scale modes is not adequate and it is necessary to include small scale modes. One large scale equilibrium solution may be unstable with respect to another large scale equilibrium solution due to small wavelength pertur-

bations. If the expansion of the equations of motion does not include these small modes, both equilibrium solutions will appear to be stable when in fact one is unstable. In our computations, we have included enough modes so that the largest of the perturbations has a viscous dissipation timescale that is $\sim 10^4$ times smaller than the dynamic timescale. It is therefore unlikely that the steady-state solution that we have computed is unstable with respect to any of the neglected small modes. The only other study of convection that has a spatial resolution equivalent to ours was done by Gilman (1978, and references cited therein). Unfortunately, it is impossible to make direct comparisons to Gilman's work because his calculation is for a rapidly rotating shell fluid in which the coriolisis force is roughly the same strength as the convective buoyancy. His solutions favor no spatial symmetry and are time-dependent.

Perhaps the most interesting result presented in this paper is that for the first time we have been able to calculate the kinetic and thermal energy spectra as functions of wavelength by solving the equations of motion alone. (For a somewhat similar derivation of a kinetic spectrum by use of an eddy viscosity, see Siggia and Patterson, 1978.) We have seen that the kinetic energy is so quickly dissipated by viscosity that it does not have time to cascade from the large modes down to smaller modes. Since the thermal dissipation rate is slower than the viscous dissipation rate, it is reassuring that our calculations show that the thermal energy does have time to cascade down to smaller wavelength before it is dissipated.

REFERENCES

Busse, F.H. 1975, J.Fluid Mech., 72, 67.

Corrsin, S. 1964, Phys. Fluids., 7, 1156.

Gilman, P.A. 1978, Geophys. Ap. Fluid Dynamics, 11, 191

Herring, J.R. 1963, J.Atm.Sci., 20, 325.

Lorenz, E.N. 1963, J. Atm. Sci., 20, 130.

Malkus, W.V.R., and Veronis, G. 1958, J. Fluid Mech., 4, 225.

Marcus, P.S. 1979, Ap. J., 231, 176 (Paper I).

Marcus, P.S. 1980, submitted to Ap.J.

Siggia, E.D., and Patterson, G.S. 1978, J. Fluid Mech. 86, 567.

Tennekes, H., and Lumley, J.L. 1972, A First Course in Turbulence,
    (Cambridge, MA: MIT Press).

Toomre, J., Gough, D.O., and Spiegel, E.A. 1977, J. Fluid Mech.,
    79, 1.

Toomre, J., Zahn, J.P., Latour, J., and Spiegel, E.Q. 1976, Ap. J.,
    207, 545.

FIGURE CAPTIONS

Figure 1 - The mean temperature gradients for conductive equili-
brium (dotted line) and convective equilibrium (solid line)
as a function of radius. The derivatives of both gradients
are discontinuous at $r = 0.3$, the outer boundary
of the heat source. The convective gradient is nearly iso-
thermal outside of $r = 0.3$ and is positive for $0.55 < r$
< 0.86.

Figure 2 - The ratio of the convective heat flux to the total
(convective and conductive) flux. For $0.55 < r < 8.6$,
the ratio is greater than 1, which means that conduction
carries energy <u>downward</u> in this region.

Figure 3 - The mean temperature of the convecting fluid as a
function of radius. The temperature of $r = 1$ is zero due
to boundary conditions. The central temperature is free
to vary and the convective flux has reduced it from its
value of 4.0 in conductive equilibrium to 0.68 in convec-
tive equilibrium. The boundary layer at $r \approx 0.88$ and the
boundary of the heat source at $r = 0.3$ are apparent.

Figure 4 - The kinetic energy spectrum at $r = 0.5$ for Reynolds
number ≈ 3 as a function of ℓ. The spectra shows a nearly
exponential decay with no trace of a production or equili-
brium range. The slight curl upward at $\ell = 12$ is due to trun-
cation.

Figure 5 - The thermal energy spectrum at r = 0.5 as a function
of ℓ for a Peclet number of $\tilde{}34$. The thermal spectrum
falls off less steeply than the corresponding kinetic
energy spectrum. The flatness of the spectrum at $\ell \lesssim 3$

is due to a combination of production and cascade of ther-
mal energy. The upward curl at $\ell=12$ due to truncation is
more severe in this figure than it is in figure 4 for the
kinetic energy.

Figure 6 - The kinetic energy spectrum as a function of $(k\eta)^{4/3}$
where k is the 3-dimensional wave number and η is the
Kolmogorov length. By fitting the slope of this calculated
curve for $4.0 \lesssim r \lesssim 8.0$ to the theoretical dissipation spec-
trum $KE(k) \propto \exp[-3\alpha(k\eta)^{4/3}/2]$, we have computed the dimen-
sionless constant α to be 3.07.

Figure 7 - The fraction of the convective flux at r = 0.5 carried
by all modes with horizontal wave number ℓ is plotted as a
function of ℓ. Nearly 90% of the convection flux is carried
by the $\ell = 1$ mode. Like the thermal and kinetic energy spec-
tra, the convective flux decreases exponentially with
increasing ℓ.

Figure 8 - The fraction of the total amount of kinetic (thermal)
energy that is produced in the ℓth shell of modes is shown
by the solid (open) circles. While 93% of the kinetic
energy is produced by the $\ell = 1$ mode, only 73% of the ther-
mal energy is produced by that mode. The figure shows that
the production of thermal energy is more important than the
production of kinetic energy in high ℓ-shells.

Figure 9 - The ratio of the kinetic (thermal) energy that is vis-
cously dissipated by the ℓth shell of modes divided by the
amount of kinetic (thermal) energy that is produced in the
ℓ^{th}-shell is plotted as solid (open) circles. The ratio
for the kinetic energy is near unity for all ℓ and is indica-
tive of no kinetic energy cascade; all of the kinetic energy
produced in the ℓth shell is dissipated there before it has
a chance to cascade to a different ℓ shell. For $\ell = 1$ the
ratio for the thermal energy shows that more energy is pro-
duced there than dissipated; this indicates that thermal
energy escapes from the $\ell = 1$ shell by cascading into higher
ℓ shells. For $\ell \geq 2$ the thermal ratio is greater than 1
and increases exponentially indicating that the ℓth shell
dissipates more thermal energy than it produces. The extra
energy that is dissipated is provided by the energy cascade.

Figure 10 - The radial component of the $\ell = 1$ velocity as a func-
tion of radius. The velocity has been normalized by its
maximum value of   33.8. The velocity shows no trace
of the boundary of the heat source at $r = 0.3$.

Figure 11 - The $\ell = 1$ component of the temperature as a function
of radius. The temperature is normalized by its maximum value
of .0226. The temperature has an obvious peak at the boundary
of the heat source.

Figure 12 - The kinetic energy spectra $KE(\ell,r)/r^2$ as functions
of radius for $\ell=1,12$. As ℓ increases the spectra peak at
increasing values of the radius. The edge of the outer boun-
dary layer is approximately equal to the radius of the
local minimum of $KE(\ell,r)/r^2$ near $r = 1.0$. For $1 < \ell \leq 6$ the
thickness of the layer decreases slowly with increasing ℓ.
For $\ell > 6$ the thickness is nearly constant.

Figure 13 - The thermal energy spectra $TE(\ell,r)/r^2$ as a function
of radius. As ℓ increases, the radii of the maximum values
of these spectra increase. For $\ell < 6$ there is
a secondary peak near the edge of the boundary layer. At
$\ell = 6$ the two peaks merge and for higher ℓ only one peak
can be seen. There is more radial structure in the thermal
than in the kinetic energy spectra because the thermal fluc-
tuation are less easily dissipated when the Prandtl number
is greater than 1.

Figure 14 - The ratio of the horizontal to the radial component
of the kinetic energy for $\ell = 1$. The ratio is a measure of
the large scale anisotropy of the flow.

Figure 15 - Same as figure 15 except that this figure is for the $\ell = 2$
component of the velocity. The anisotropy for $\ell = 2$ is quali-
tatively the same for $\ell > 2$ and there is no apparent isotro-
pization of the velocity at small wavelengths.
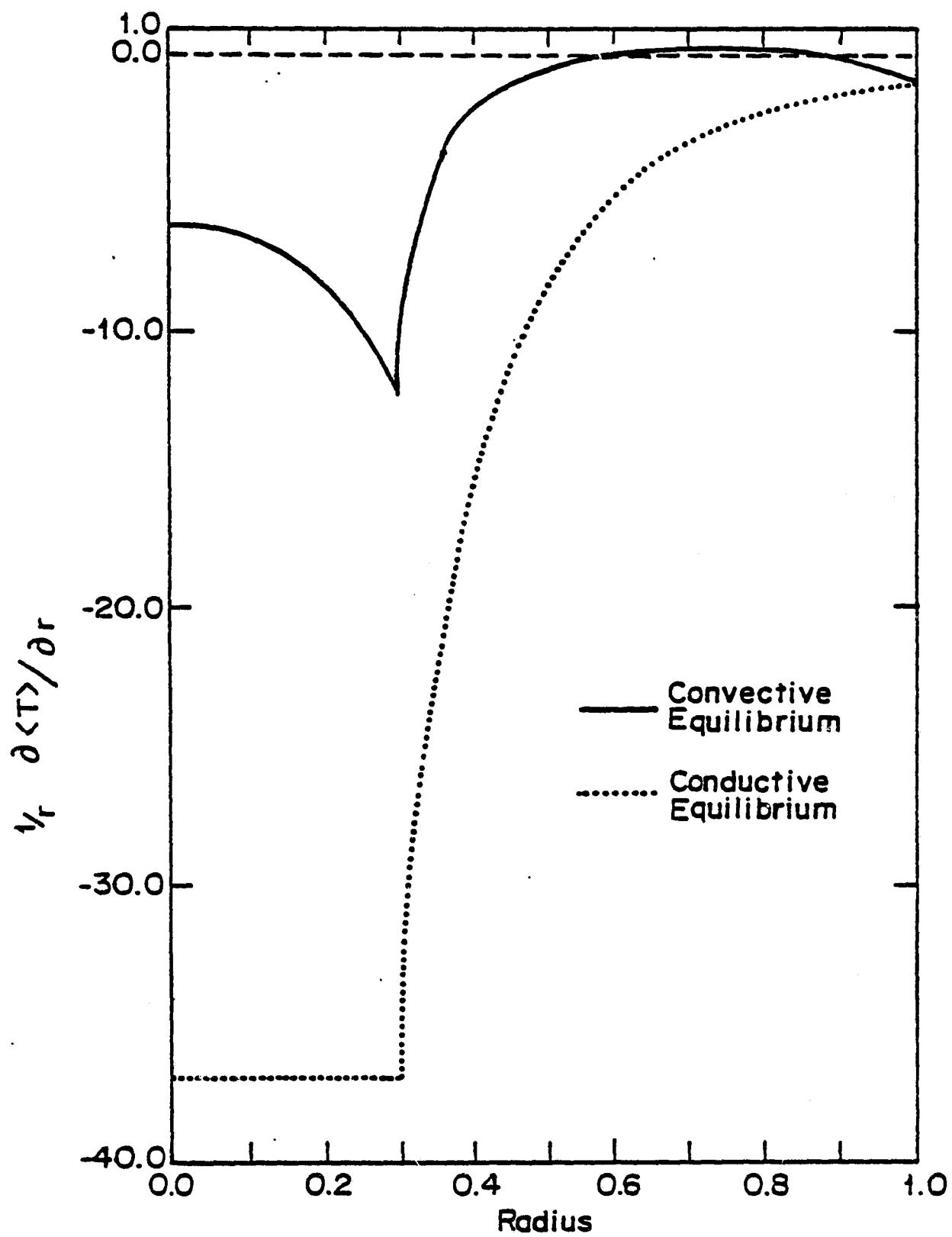
Figure 1

Figure 2

Figure 3

r = 0.5

KE (ℓ, r)

ℓ
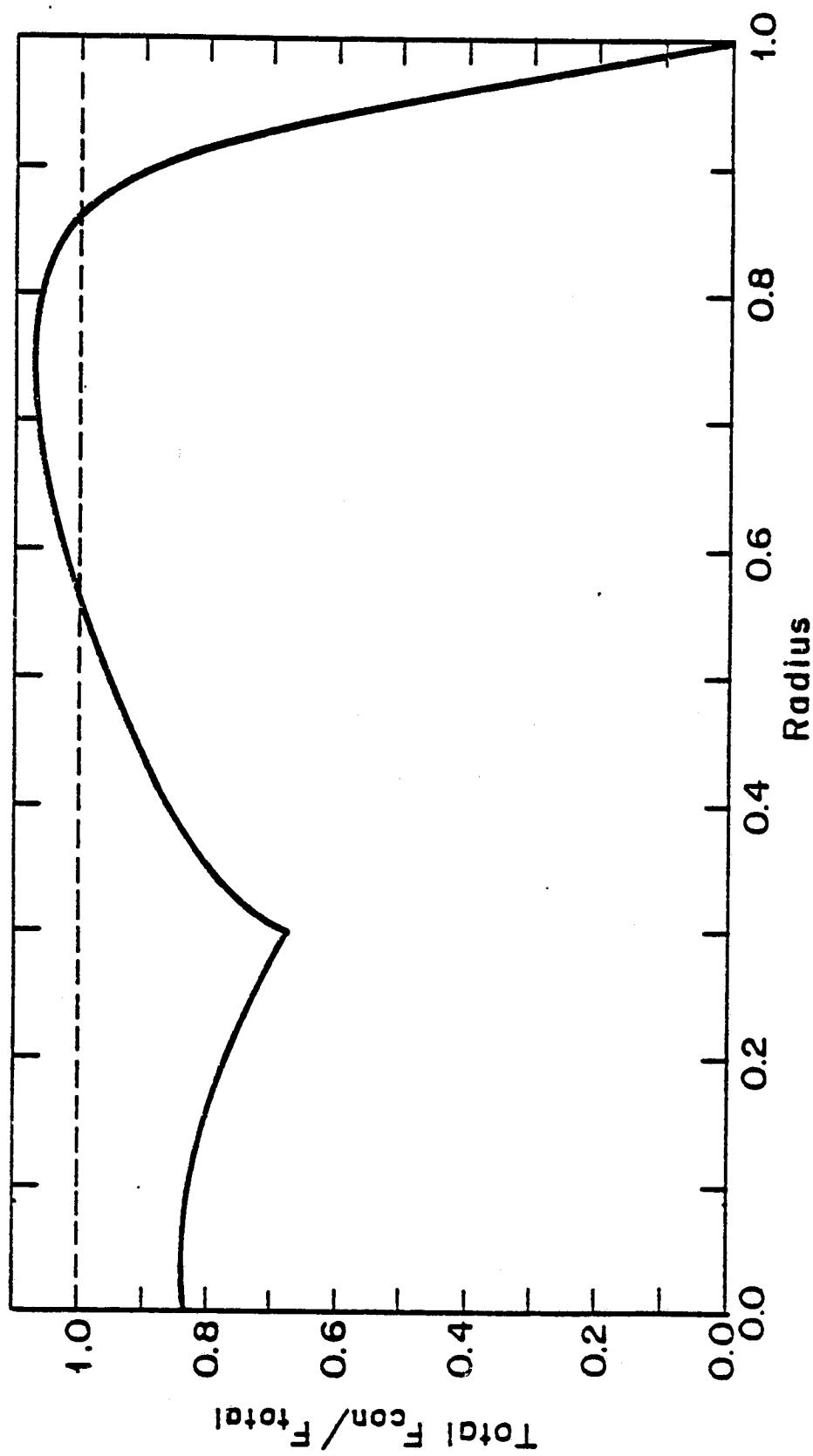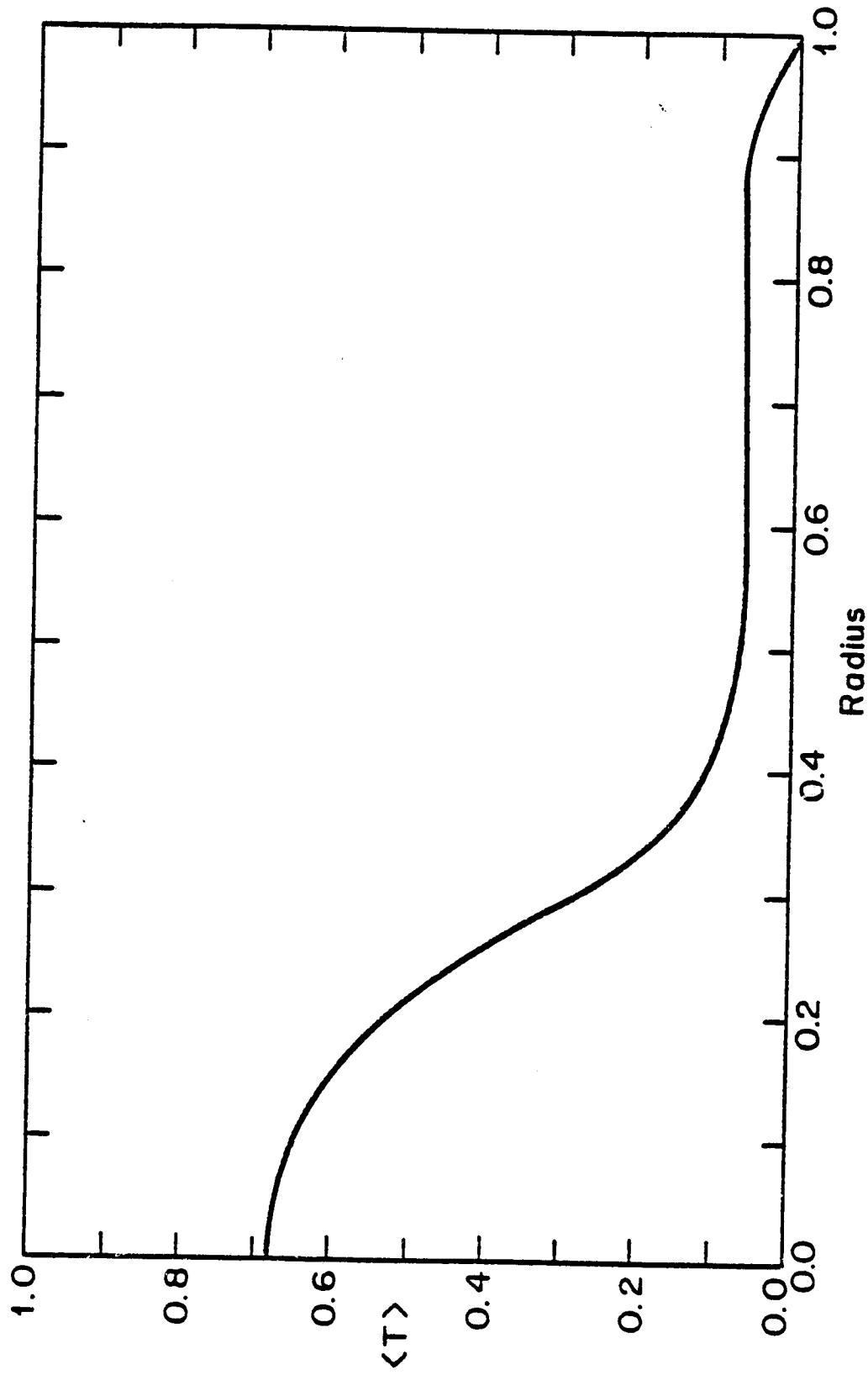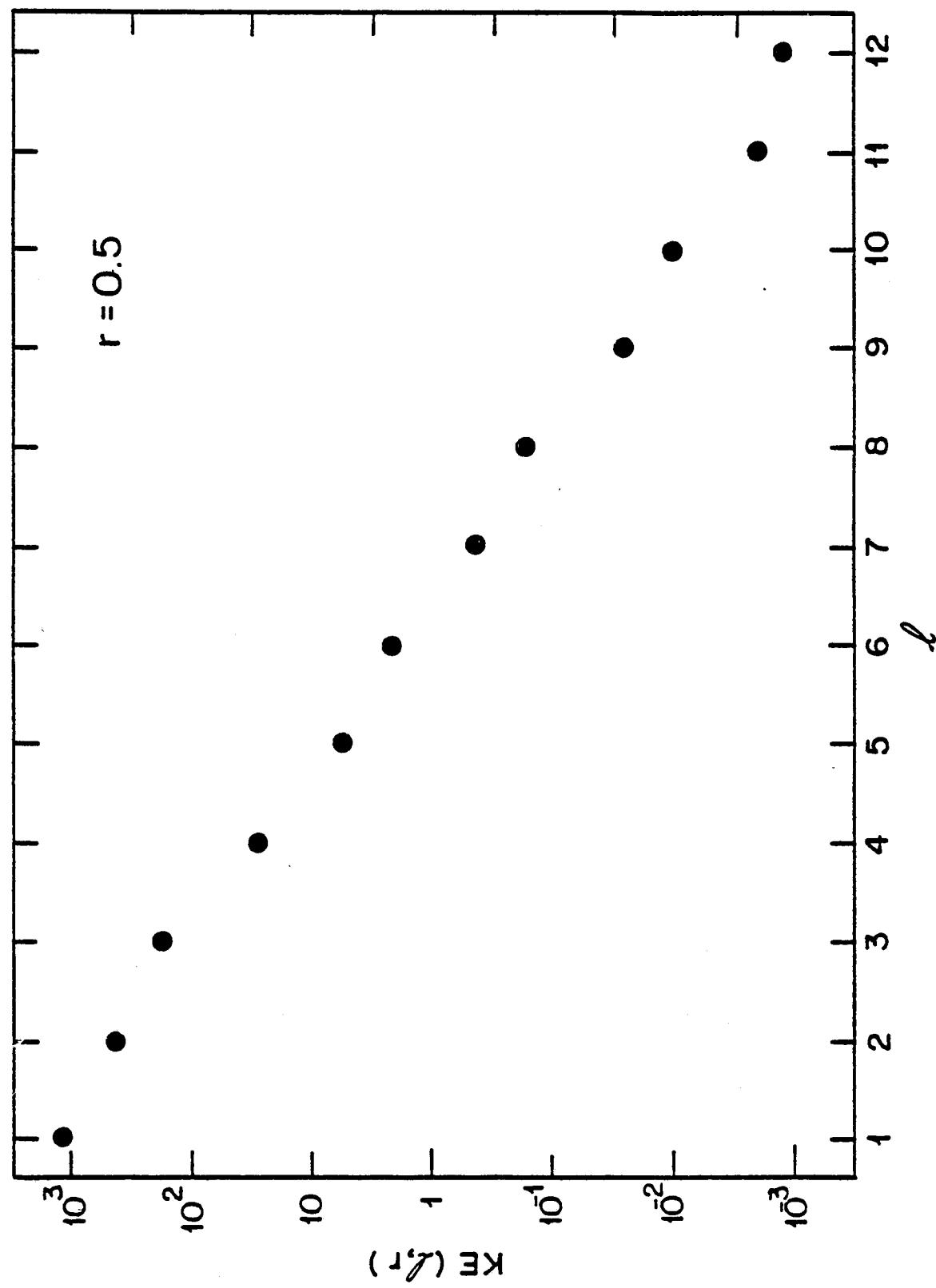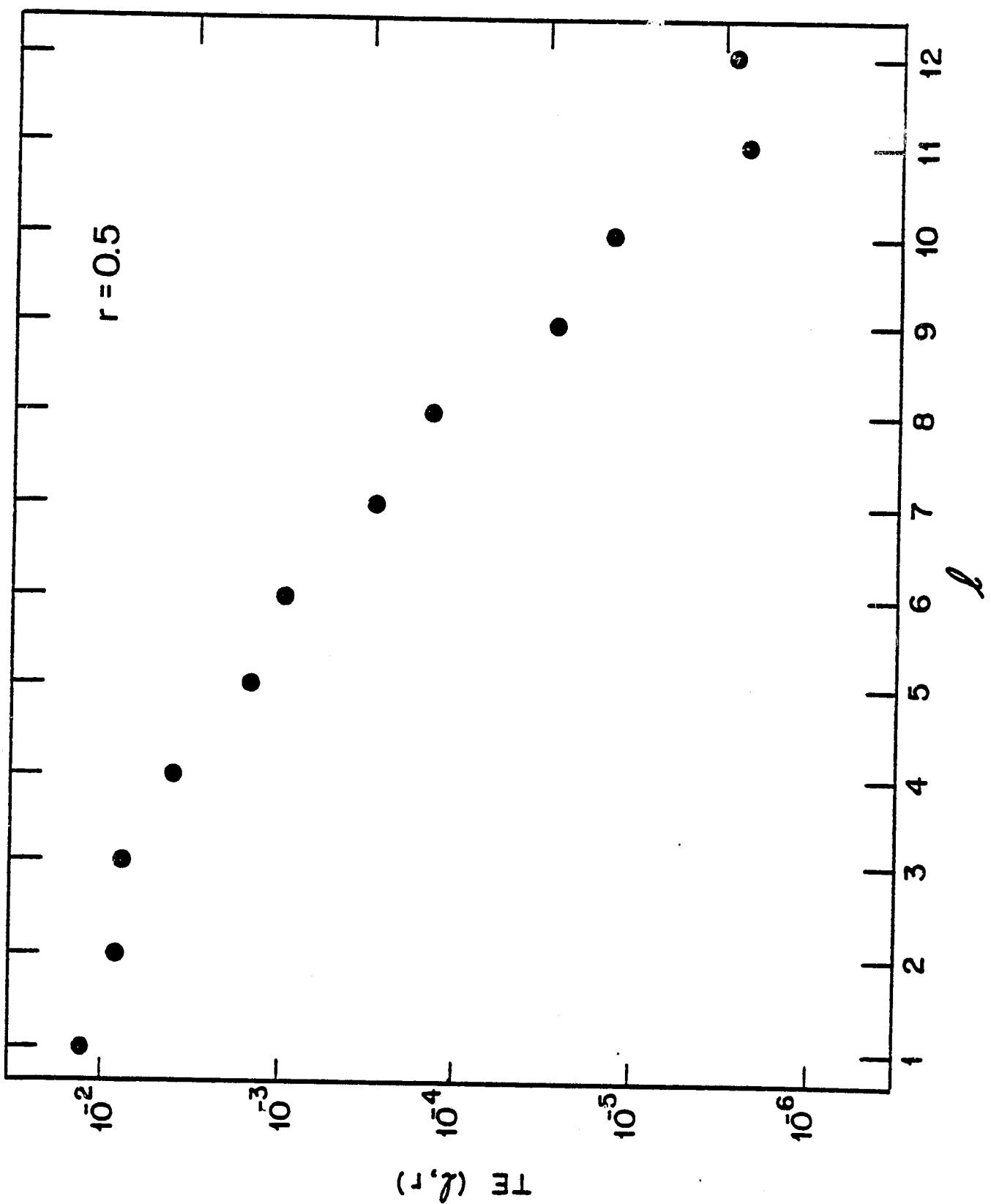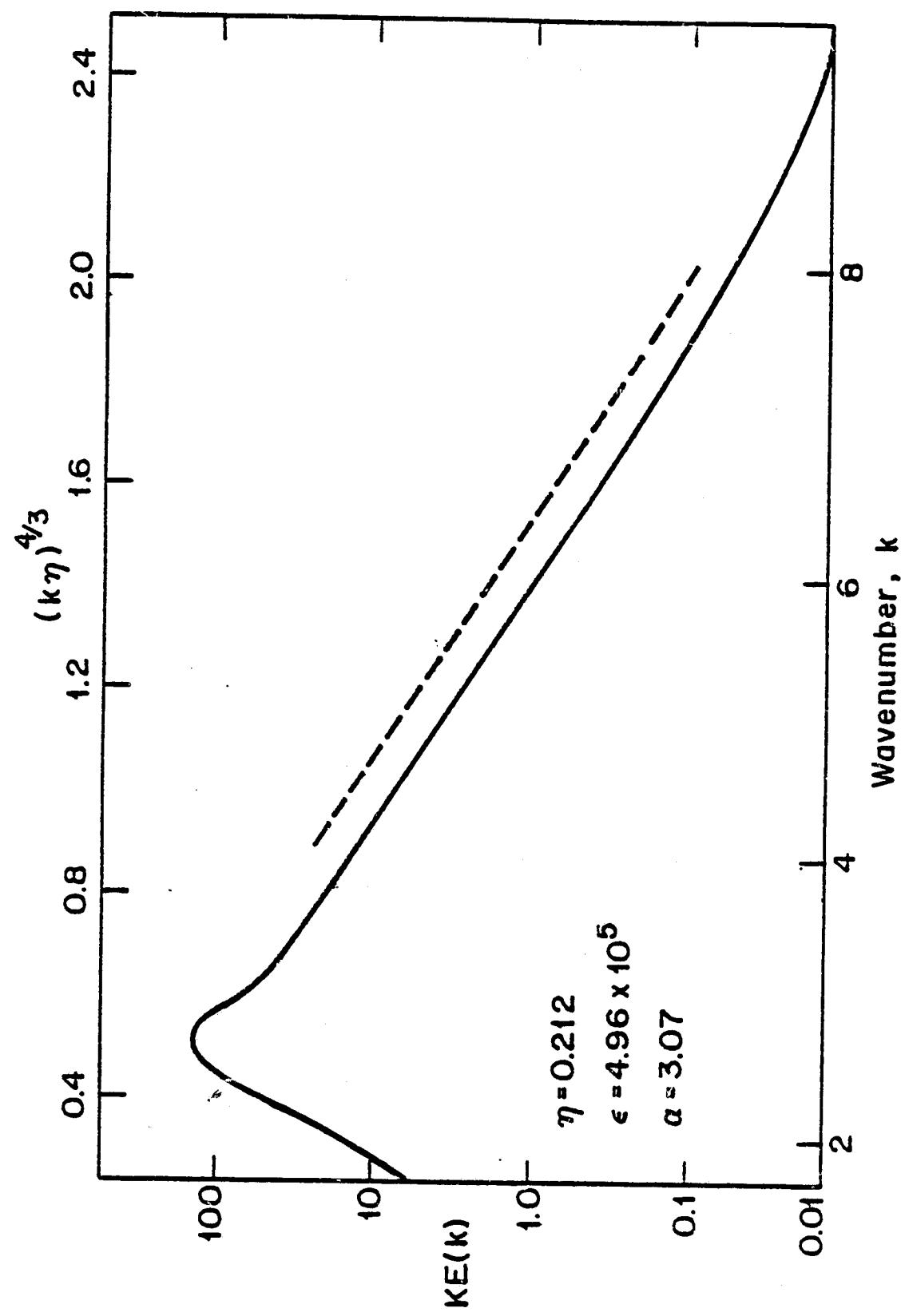
Figure 4

Figure 5

Figure 6
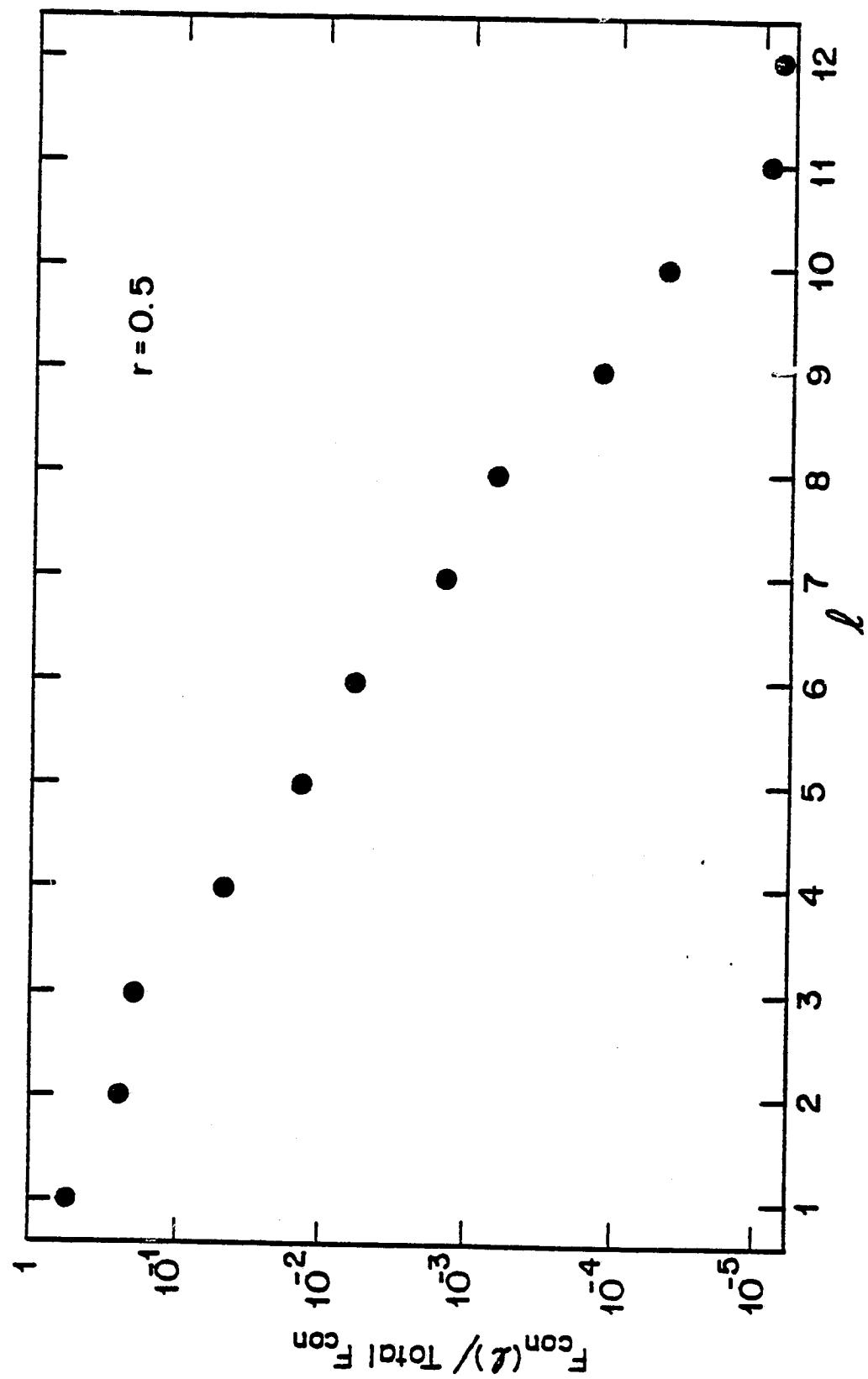
Figure 7
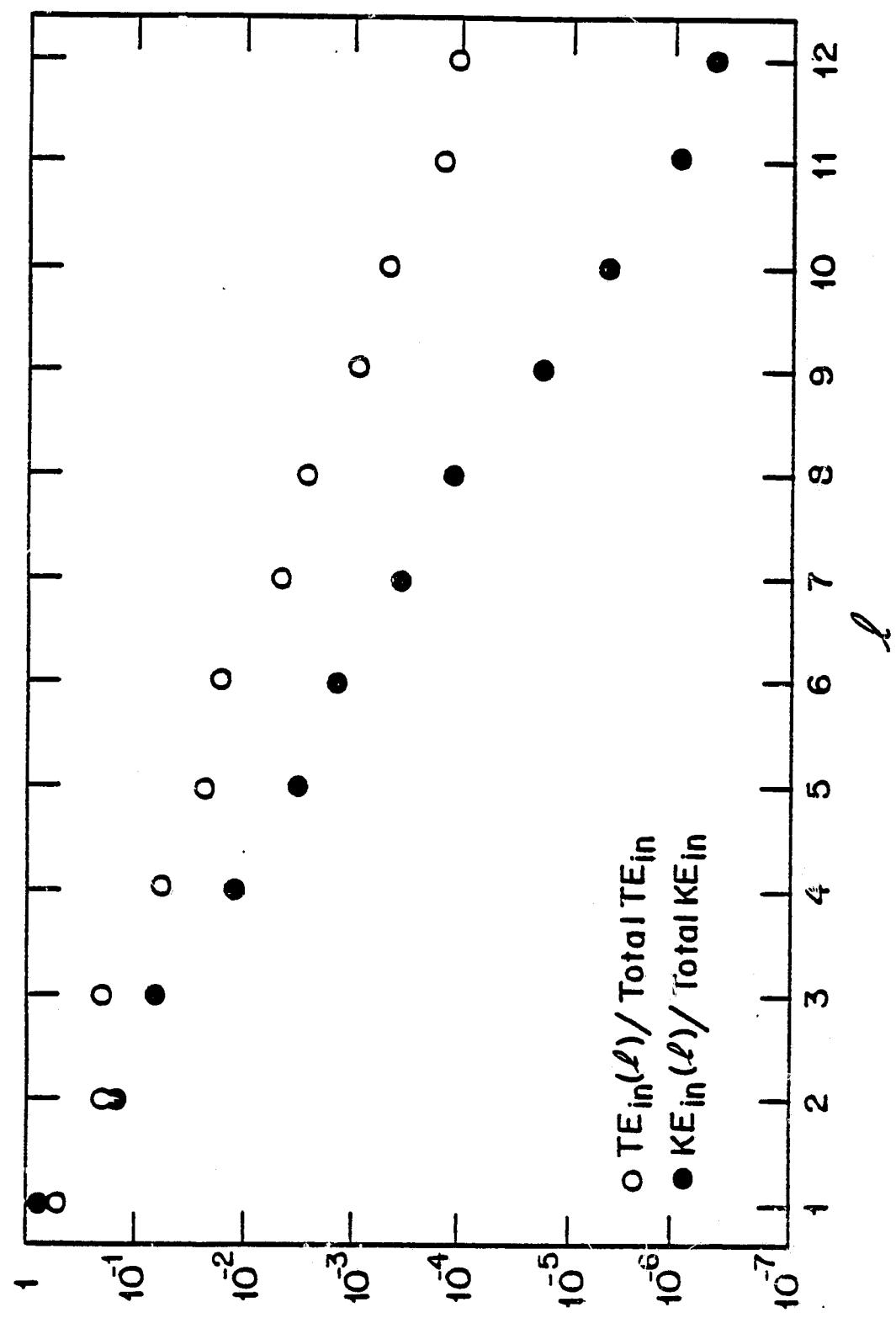
Figure 8
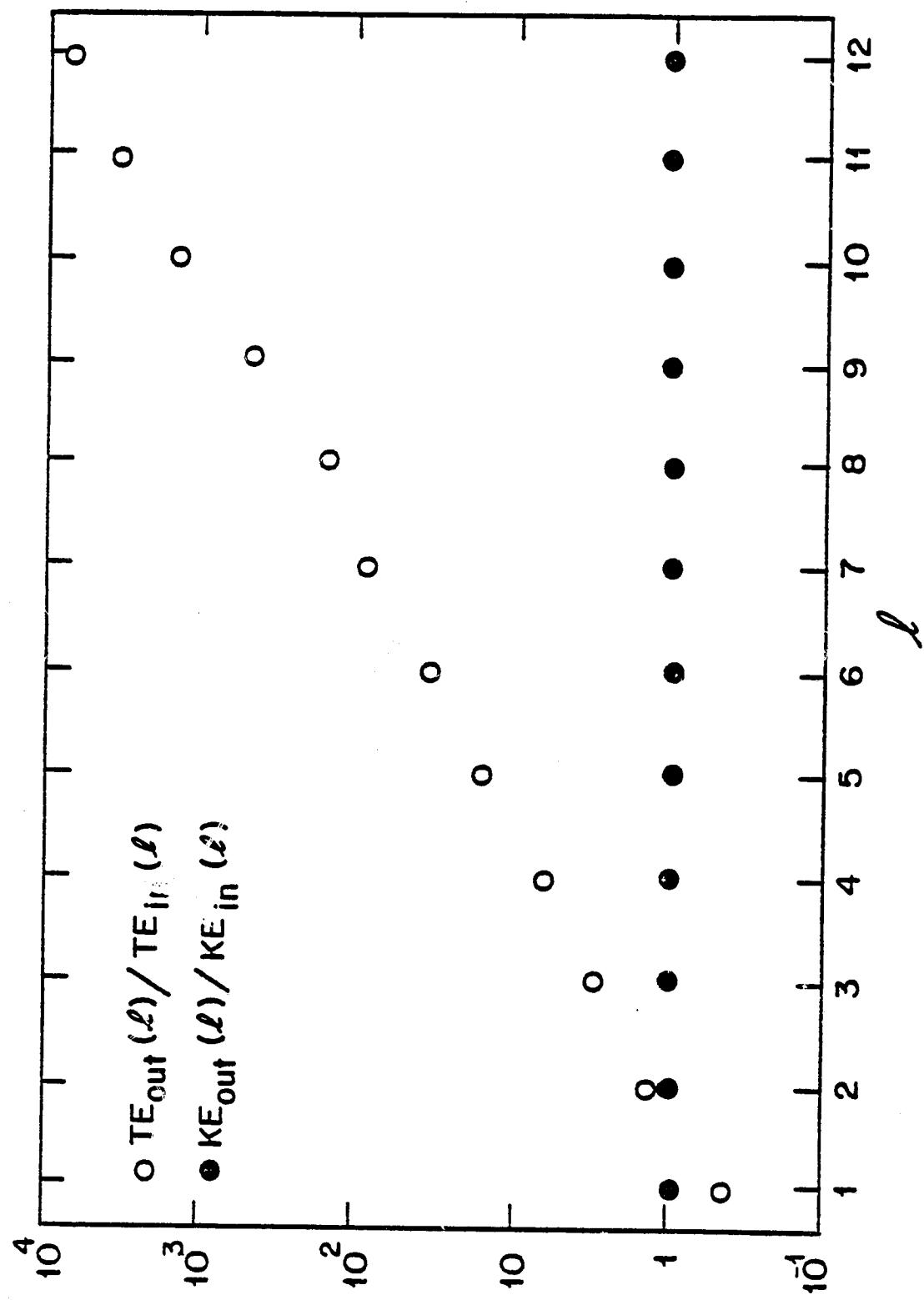
Figure 9
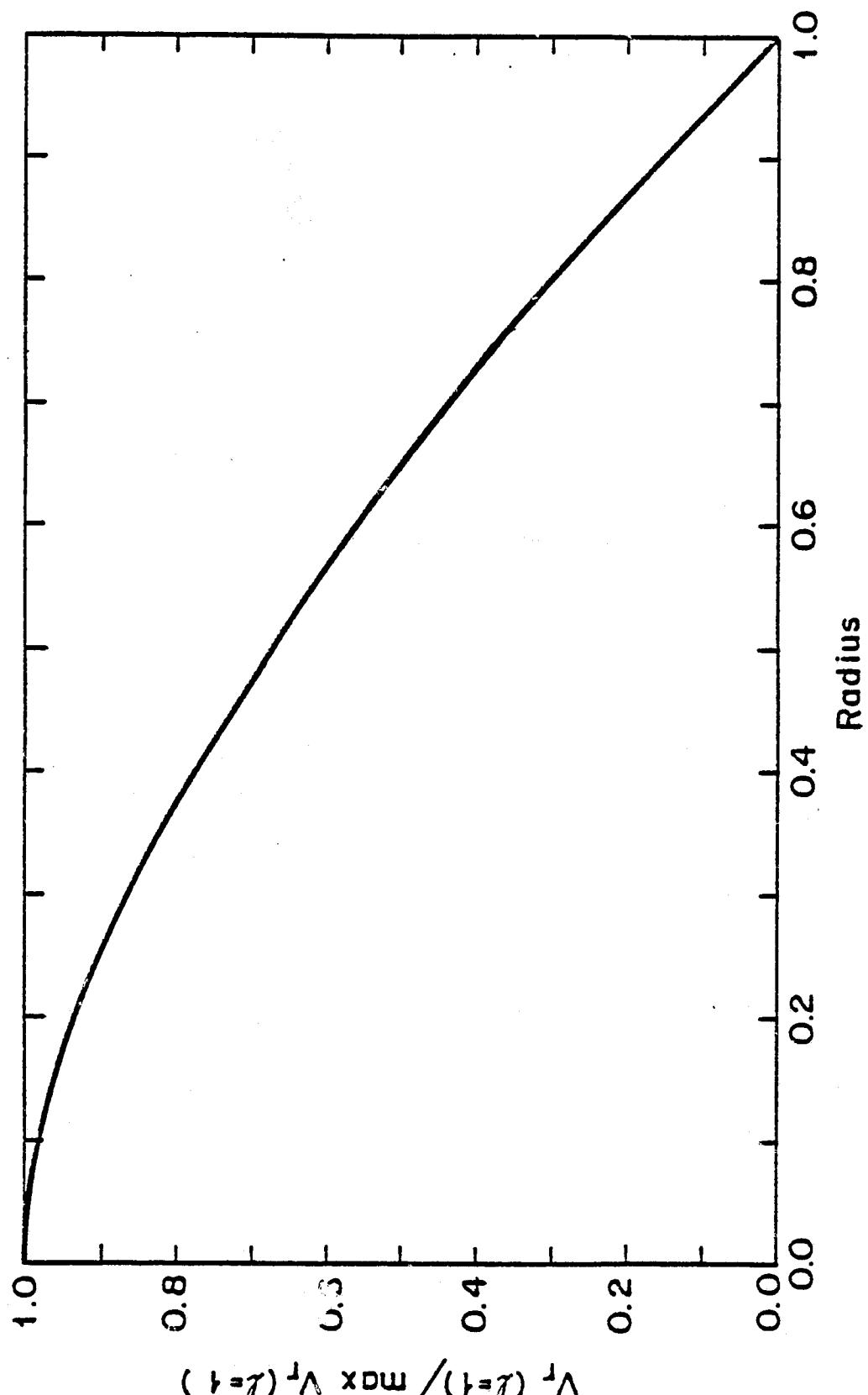
Figure 10
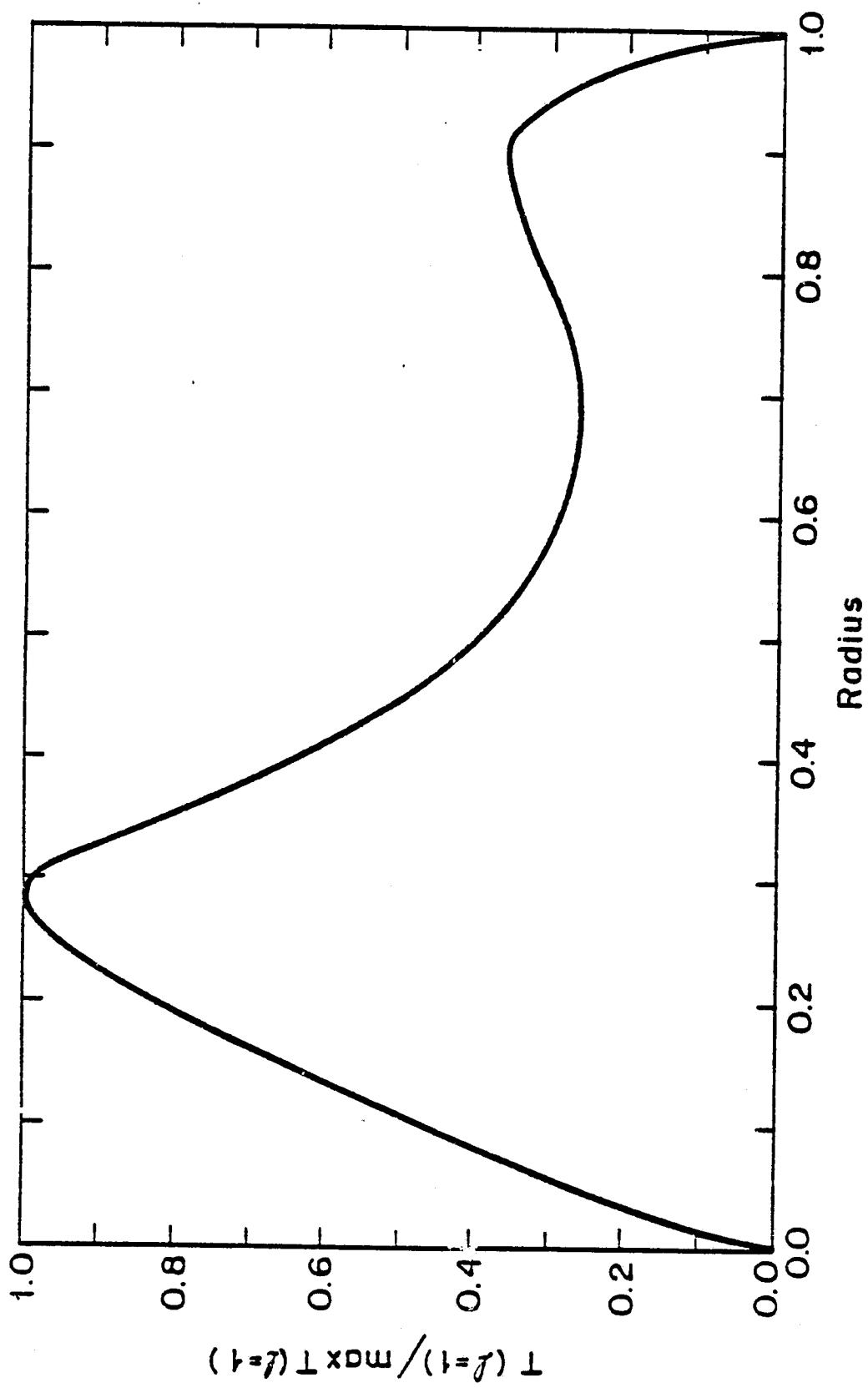
Figure 11
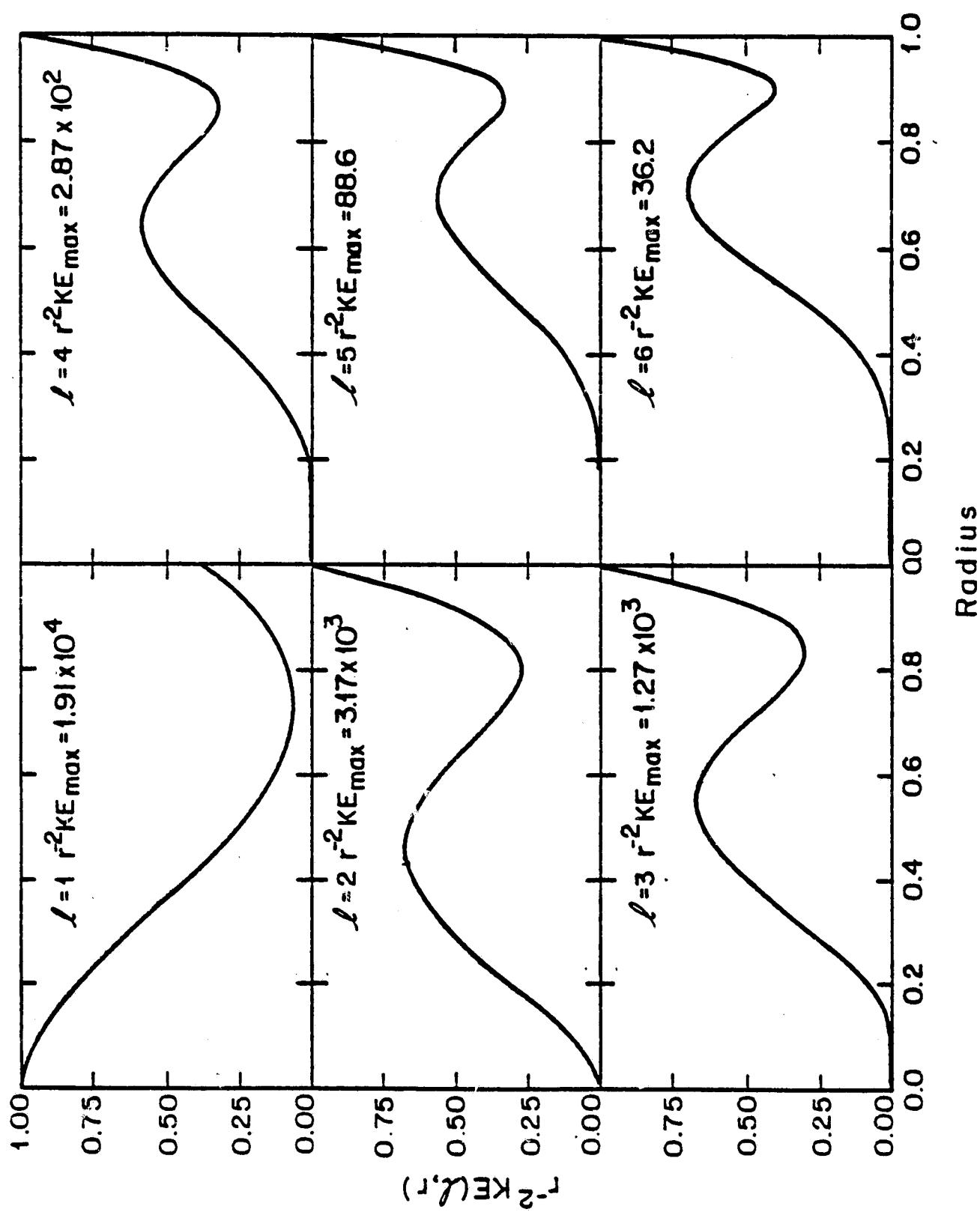
Figure 12a
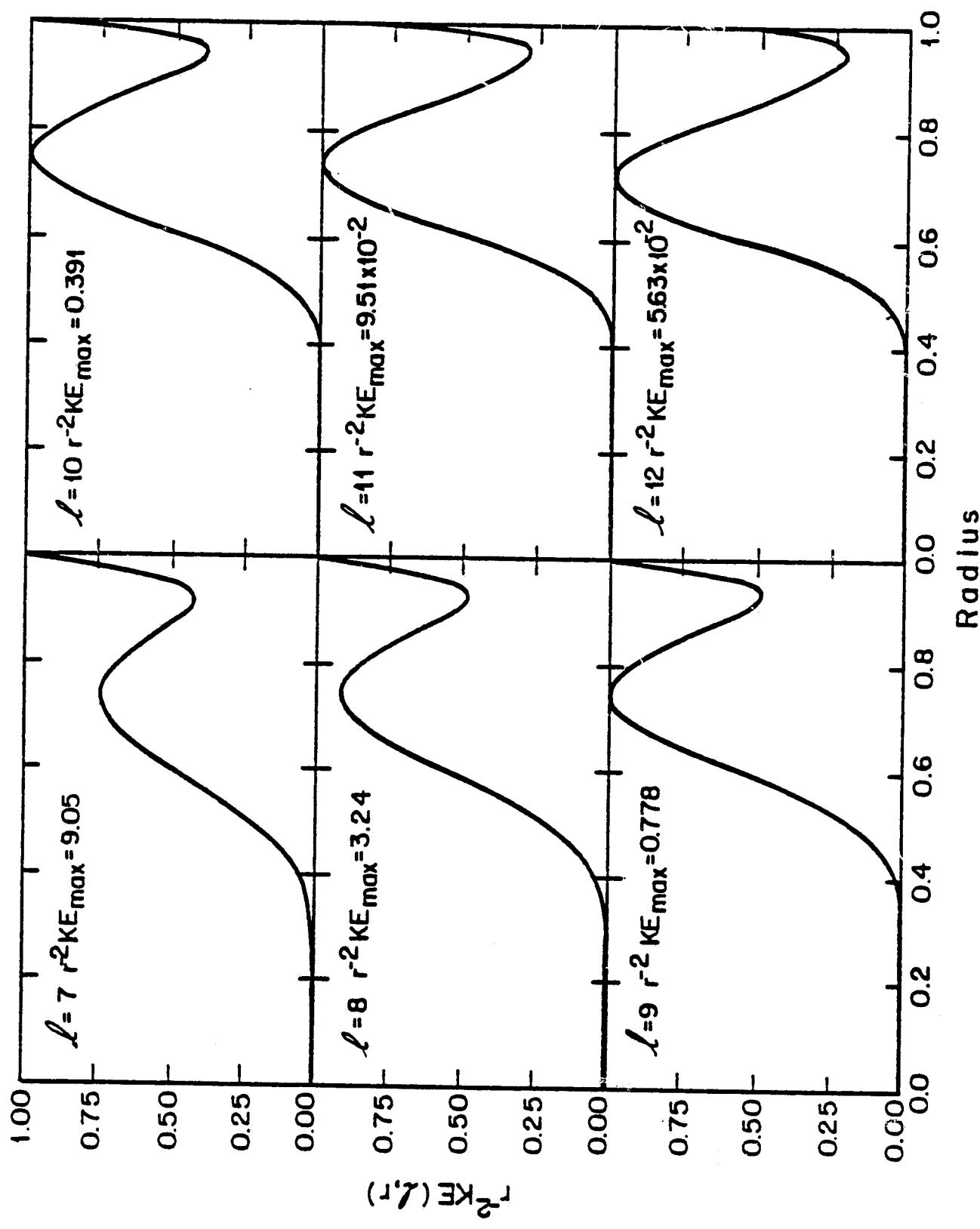
Figure 12b
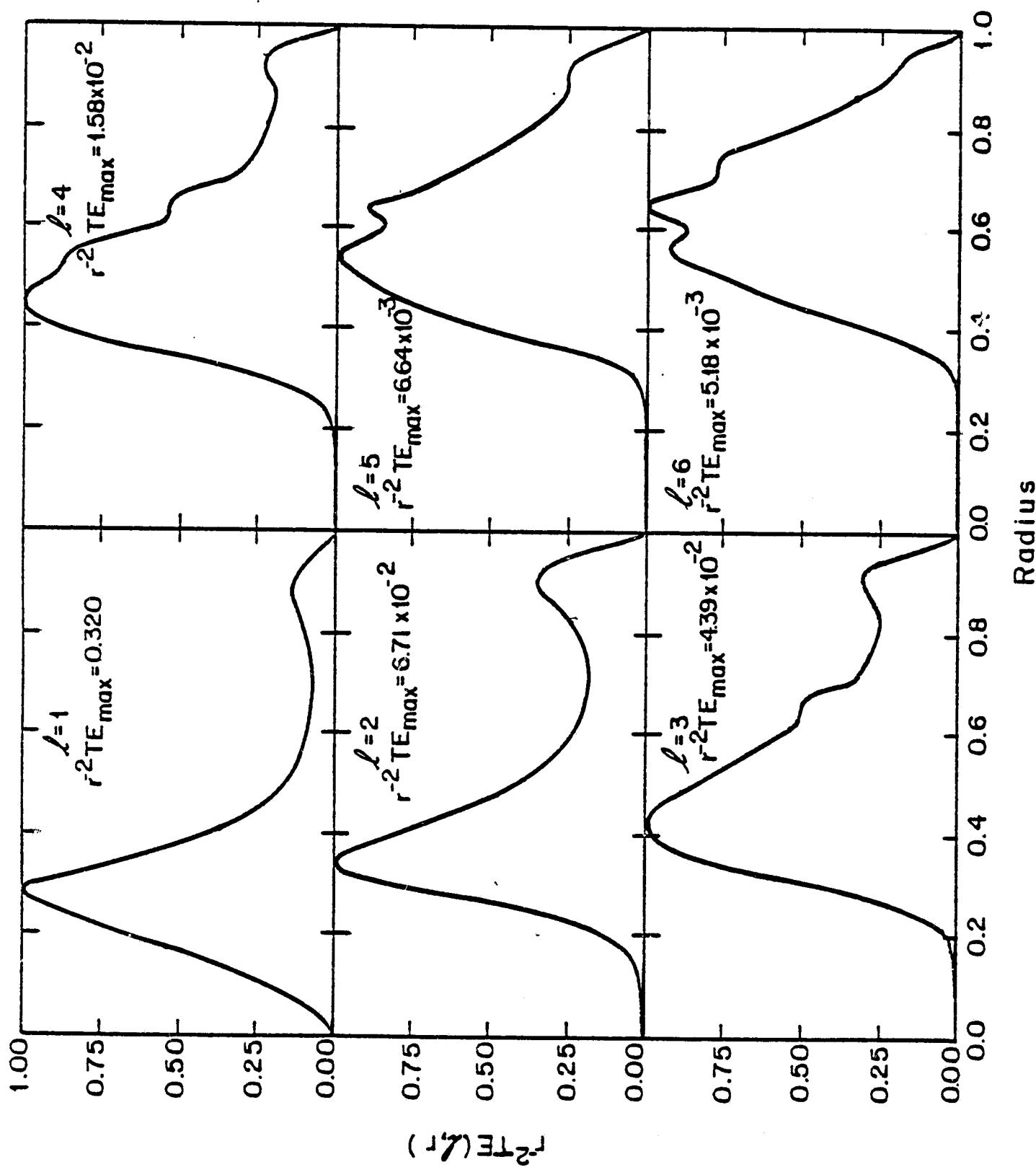
Figure 13a
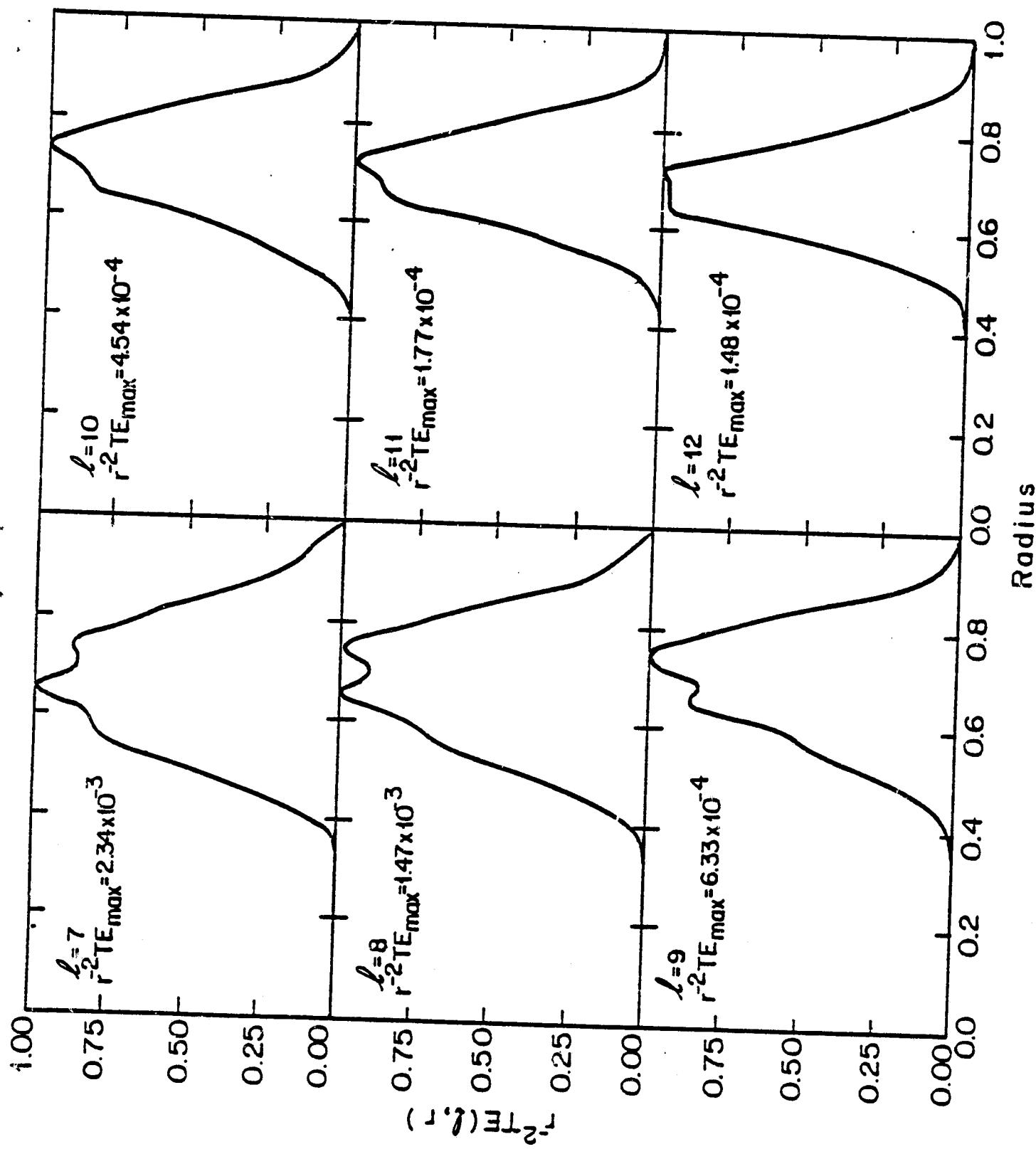
Figure 13b
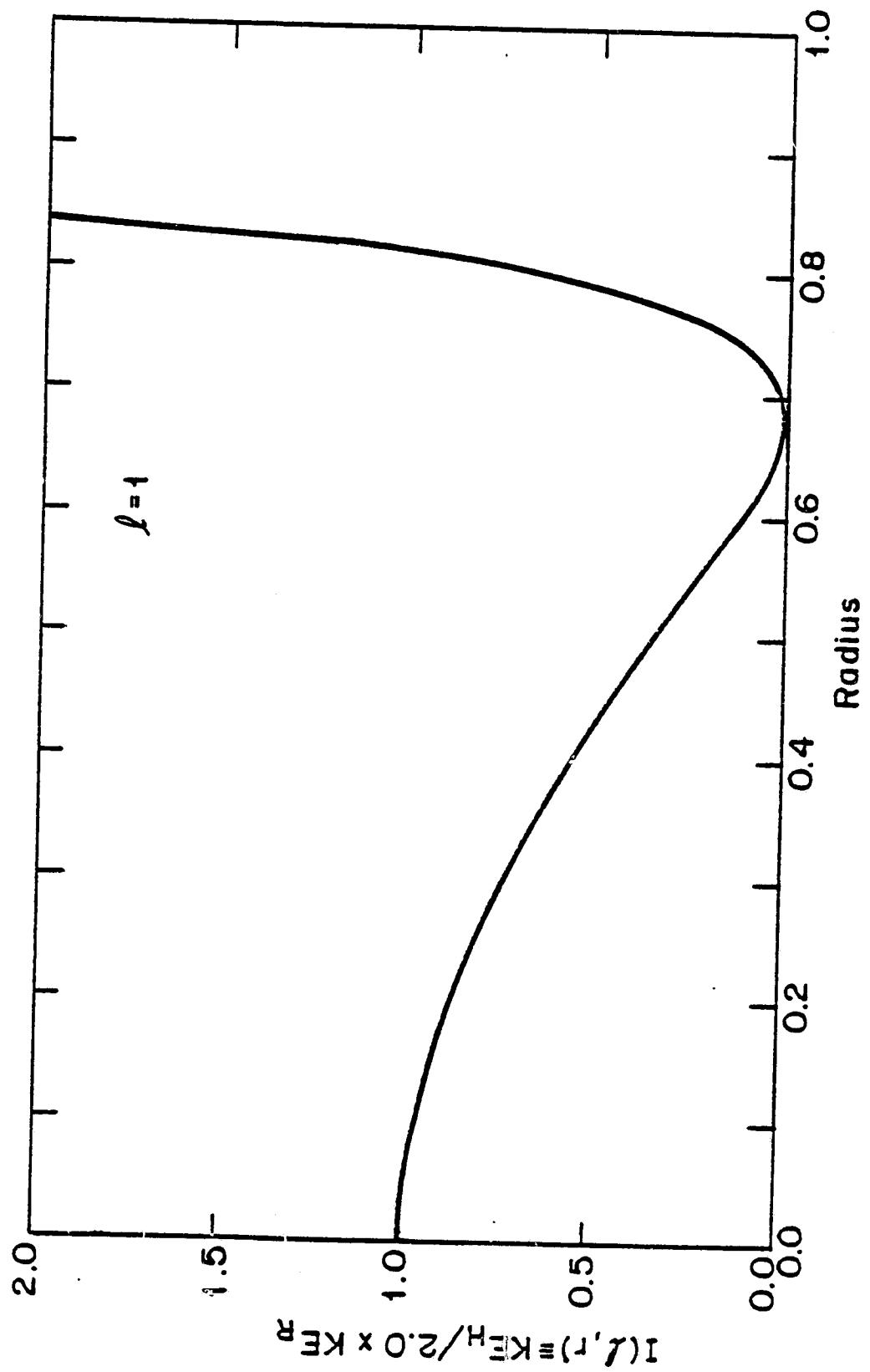
Figure 14
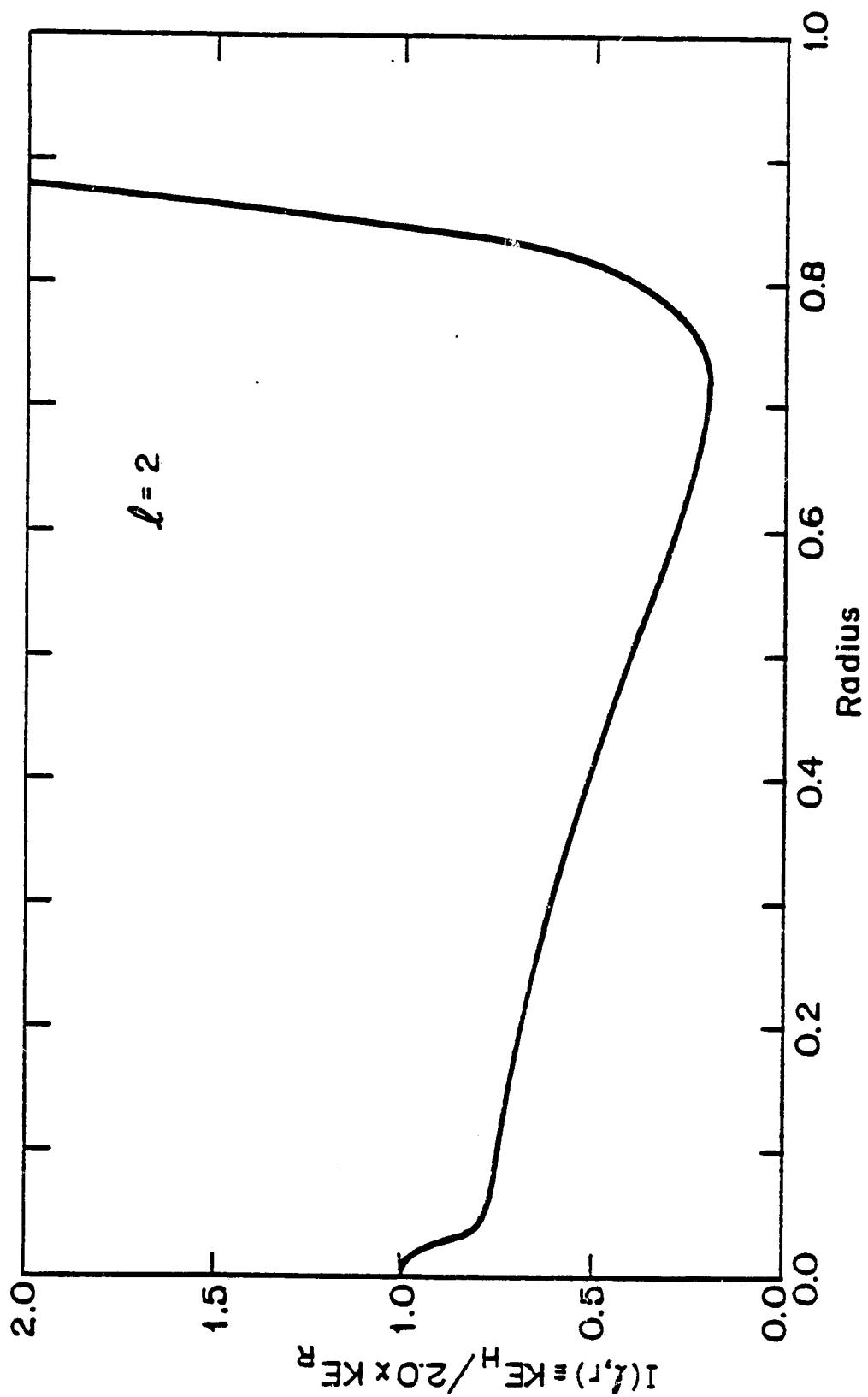
Figure 15

AUTHOR'S ADDRESS

PHILIP S. MARCUS

CENTER FOR RADIOPHYSICS AND

SPACE RESEARCH

CORNELL UNIVERSITY

ITHACA, NEW YORK 14853